Commissioning of the Trigger module for the 12 GeV era experiment E12-06-114 at JLab

A thesis presented to

the faculty of

the College of Arts and Sciences of Ohio University

In partial fulfillment

of the requirements for the degree

Master of Science

Norman S. Israel

December 2014

This thesis titled

Commissioning of the Trigger module for the 12 GeV era experiment E12-06-114 at JLab

by

NORMAN S. ISRAEL

has been approved for

the Department of Physics and Astronomy

and the College of Arts and Sciences by

Julie Roche

Associate Professor of Physics

Robert Frank

Dean, College of Arts and Science

Abstract

ISRAEL, NORMAN S., M.S., December 2014, Physics

Commissioning of the Trigger module for the 12 GeV era experiment E12-06-114 at JLab

(73 pp.)

Director of Thesis: Julie Roche

Generalized Parton Distributions are a powerful new tool to study the position and momentum distribution of quarks and gluons inside hadrons. The simultaneous position and momentum distribution of quarks and gluons within the nucleon are barely known and unraveling them would lead to a deeper understanding on the structure of hadrons. Deep Virtual Compton Scattering (DVCS) is currently the best known process to access GPDs as it provides the simplest final state and thus the simplest understanding of nucleon structure. The E12-06-114 experiment, which will begin in October 2014, will focus on completing the proof that in the DVCS process, one is indeed scattering off of a single quark. This thesis focuses on the preparation of the trigger module for this experiment. The 208 channel level-2 trigger module will help reduce acquisition dead-time in the experiment. This FPGA based trigger is designed to help meet the goal of achieving a systematic error of 4%. The work done for this thesis involved integrating the module within the standard Data Acquisition System used at JLab (CODA) and testing its basic functionalities. By the end of this work, data were taken with CODA simultaneously with the trigger module and the dedicated fast ADC used by the experiment. The basic functionality of this level-2 trigger was demonstrated.

To those who encouraged and assisted me along the way.

Acknowledgments

This material is based upon work supported by the National Science Foundation under Grant Award #1306376. Any opinions and conclusions or recommendations expressed in this material are those of the author and do not necessarily reflect the views of the National Science Foundation (NSF).

Table of Contents

List of Tables

List of Figures

1 Introduction

In ancient Greece, natural philosophers such as Democritus, Epicurus, etc, held the view that the universe is composed of 'indivisible' objects they called atoms. They developed a systematic philosophy of explaining the origins of things within the universe from the interaction of these 'indivisible' objects as they strike, rebound and interlock in the infinite void [Ber11]. Today, it is well supported that atoms are not indivisible, but consists of a cloud of negative charge surrounding a positive core - which contains protons and neutrons; nucleons. The interaction of a nucleon with a nucleon, or an electron with a nucleon are some of the ways used today to probe even deeper into the structure of matter to glimpse a much more rich and exciting part of nature viewed through the goggles of particles and their interactions. The foundation of this view of nature is worked out in quantum mechanics but the intuition that lead to the modern view of particles and interactions began with Michael Faraday [Rov04]. This intuition is the field. Faraday viewed the field as lines of force filling space as they emanate from a source (e.g a positive charge, the North pole of a bar magnet). This intuition was then formalized by James Clerk Maxwell into a classical field theory that unified electricity and magnetism and formally removed the notion of action-at-a-distance from classical electricity and magnetism. Many of the ideas from Maxwell's classical field theory are carefully and skillfully adapted to understand and make predictions about matter at the tiniest scales. The behaviour of matter at these tiny scales is today, empirically studied by probing how particles scatter when they collide with other particles. This means of probing the structure of matter has been enlightening, as it has revealed that the components of the core of atoms are themselves made of even smaller particles - quarks and gluons. These quarks and gluons form a 'sea' and their fundamental properties are worked out in the quantum field theory of quantum chromodynamics (QCD). Still, much is left unknown about the way quarks and gluons interact to give the form that visible matter takes.

In order to understand how the quarks and gluons interact to give visible matter, work to produce spatial-momentum distribution maps of the quarks and gluons in action is being done. This thesis focuses on the preparation of one such experiment, that uses electron-nucleon scattering (at JLab) with the aim of producing such distributions using a process called Deep Virtual Compton Scattering. The thesis is organized as follows:

- Chapter 2 - *A brief introduction to hadrons and deep virtual compton scattering (DVCS).*
- Chapter 3 - *Goals of the new Hall A DVCS experiment. The aim of this chapter is to address the question 'why should one care about doing another DVCS experiment?' In addition, there will be a discussion on the general setup of the experimental hall (Hall A) for the DVCS experiment.*
- Chapter 4 - *Commissioning of the data acquisition system for the new DVCS experiment in Hall A at JLab is the aim of this thesis. This chapter gives a brief introduction to the process of data acquisition (which will include discussions on what a trigger is and other basic components of data acquisition systems) while at the same time discussing the data acquisition system for the upcoming DVCS experiment.*
- Chapter 5 - *Main aim of the work for this thesis, which is the preparation of the trigger for the new DVCS experiment.*
- Chapter 6 - *Summary of the work and what is left to be completed.*

2 Introduction to the structure of Hadrons

2.1 Brief Review of QCD

The purpose of this chapter is to develop, from a very brief historical perspective how QCD came to the stage of development it has reached. The chapter begins with a general but in no way exhaustive discussion on some historical developments. Then, there will be some discussion, in the context of the DVCS experiment on more specialized tools that are used to probe hadron structure - GPDs. GPDs are relatively new tools to study hadronic structure and the aim of the experiment which this thesis will contribute to is to deepen understanding of the structure of hadrons by exploring hadronic structure using GPDs.

2.1.1 A Brief History of Developments

The naive atomic model [Gri04b] was unable to explain the nature of the nuclear forces. One of these forces - strong force - is viewed in the framework of a quantum field theory called quantum chromodynamics (QCD). QCD is the theory through which some of the many particles that were discovered in the period surrounding the mid 1900s and later is understood. It was realized by Murray Gell-Mann that these particles - baryons and mesons (both hadrons), could be arranged into geometrical patterns based on their electric charge and their strangeness (one of the quantum numbers for quarks). This was the so called Eight-fold Way. The Eight-fold way is a classification scheme which helped in the illumination of the nature of hadrons [Gri04a].

The geometrical patterns demanded an explanation. An explanation came through quantum mechanics with the Pauli exclusion principle. In order to explain the patterns, Gell-Mann and Zweig suggested that hadrons are composed of elementary particles called quarks - mesons being composed of two quarks while baryons being composed of three. The existence of quarks was later justified using deep inelastic scattering experiments at the Stanford Linear Accelerator Center (SLAC) [Gri04a]. There are 6 types of quarks

(called flavours) - up, down, strange, charm, bottom and top. Quarks are spin-1/2 objects and thus must respect the exclusion principle. Initially, it appeared quarks violate this principle as for example, the Ω^- is composed of 3 strange quarks and so at least 2 of them have to be in the same state. The way that was used to take Gell-Mann and Zweig's idea out of this trouble was to invent a new quantum state called colour of which there are 3 types ('red', 'blue' and 'green'). If one quark of each colour in the Ω^- is taken for example, then the exclusion principle is no longer violated. The existence of colour was justified at SLAC by comparing the ratio of the rate at which hadrons are produced in electron-positron collisions with the rate of muon-antimuon pair production in these collisions as a function of electron energy. The ratio indicated sudden jumps in the ratio as the energy is increased. The value of the plateau of these jumps are seen as the evidence for colour [Gri04a].

Quarks also possess electric charge (that are a fraction of the electron charge). The nature of the strong nuclear force (over distance scales) prevents the hadrons from breaking apart due to electromagnetic repulsion. The coupling constant (which determines the strength of the force) for the strong force (as well as the other nuclear forces) changes with distance. At small distances (where the coupling constant is less than unity), the quarks are less bounded - the strength of the strong nuclear force approaches zero as the distance between the quarks approach zero. This is called asymptotic freedom [Gri04a]. In this regime, theorists can use perturbation theory to understand what is going on quite well. At large distances (but still at the size of a hadron), the strong nuclear force increases in strength (the coupling constant α_s exceeds unity), so much so that it overpowers the electromagnetic force at these scales. In addition, it means that quarks can never be observed individually but must be bounded with at least one other quark. This is called confinement [Gri04a]. The behaviour of the strong force (at both large and small distances) is captured in the non-abelian $SU(3)$ formalism of QCD.

In the confinement regime, perturbative techniques fail. As a result, new tools have to be developed to gain a greater understanding of what occurs in this regime. Many non-perturbative approaches have been developed to explore this regime. These include using form factors to explore the spatial distribution of quarks, parton distribution functions to explore the momentum distribution of quarks and gluons. More recent approaches include Generalized Parton Distributions (GPDs). In addition, there is heavy reliance on experiment to probe this regime to guide the development of theoretical models. Experimentally, the confinement regime is probed using electron-nucleon scattering (as is the case at Jefferson Lab) as well as proton-proton scattering (as is the case at CERN) and heavy ion collisions (as is the case at the Relativistic Heavy Ion collider). The aim is to answer questions such as 'how do nucleons arise out of the dynamics of QCD?' as well as to explain the origin of the spin of the proton for example. The proton consists of 2 *u* quarks and a *d* quark which interact with each other. Evidence exists that the proton's spin partially originates from the spin of these three quarks. In addition, there is evidence that some of the spin arises from the 'sea' of quarks and gluons. The quarks that make up this 'sea' are mostly the strange quark since it is the next lightest quark relative to the u and d quarks. The contribution of both the valence quarks and the sea (to the overall spin) is measured to be about 20%. A third possibility is that the quarks and gluons have a net orbital angular momentum relative to each other and it is expected that this will contribute the remaining 80% [Gui05]. All this information is revealed when one looks at both the momentum and spatial distribution of quarks and gluons inside the nucleon. Information about such distributions are contained in the form factors (FFs) and parton distribution functions (PDFs) as well as the GPDs.

2.1.2 Form Factors, Parton Distributions and Generalized Parton Distributions

Though FFs and PDFs contain the spatial or momentum distribution information, it is important to note that they only contain that one specific form of information and not both - FFs only contain information about the spatial distribution and not the momentum distribution, while the PDFs contain the momentum distribution and not the spatial distribution. Nevertheless, the understanding of hadron structure in the context of both FFs and PDFs has seen great progress, however, any attempt to go deeper must involve convergence to FFs and PDFs in the appropriate limit. GPDs, which are a unification of both FFs and PDFs is one such attempt to move beyond the understanding gleaned from FFs and PDFs. GPDs converge to FFs and PDFs in the appropriate limits. In this section, FFs and PDFs will be briefly discussed and will give an idea of what GPDs are about. Finally, the discussion will converge to that of GPDs.

2.1.2.1 Form Factors

Form factors reveal the spatial charge and magnetic distribution inside nucleons. Since quarks are the carriers of charge inside nucleons, there is therefore a connection between form factors and the spatial distribution of quarks inside the nucleons. Form factors can be probed using elastic scattering. First, recall that if one scatter from a point particle (neglecting spin) relativistically, one can compute the differential cross-section using the Mott formula

$$\left(\frac{d\sigma}{d\Omega}\right)_{point} = \left(\frac{\alpha\hbar}{2k^2\sin^2(\theta/2)}\right)^2 \left[(mc)^2 + k^2\cos^2(\theta/2)\right] \tag{2.1}$$

where θ is the scattered angle of the incoming particle, k is the 3-momentum of the incident particle and α is the fine structure constant. Eq. (2.1), can relate the differential cross-section of a composite particle with the form factor ($F(t)$, where t is the momentum

transferred to the nucleon) as

$$\frac{d\sigma}{d\Omega} = \left(\frac{d\sigma}{d\Omega}\right)_{point} |F(t)|^2 \tag{2.2}$$

The two types of form factors - electric form factor and the magnetic form factor - map out the distribution of electric charge and magnetic moment inside the nucleon. The proton's electric and magnetic form factors were measured for the first time in 1955 by R. Hofstadter and were used to determine the size of the proton [Cam05b].

In order to have a complete picture of the structure of nucleons, one not only needs the spatial distribution of the elementary constituents, but also a momentum distribution in order to catch the constituents in action. This is done using Parton Distribution Functions (PDFs).

2.1.2.2 Parton Distribution Functions

Before the quark model, the idea that hadrons could be described by point-like objects at sufficiently high energies was put forth in a model by Richard Feynman. Recall that at higher energies, one probes shorter distances. Hence, in this model, one is concerned with the components of hadrons. The model is called the parton model. One can probe these short length scales using deep inelastic scattering experiments [Gri04a]. In Fig. 2.1, the process occurring in these deep inelastic scattering experiments is shown. Here, an electron of 4-momentum (k) exchanges a virtual photon of 4-momentum (q) with a hadron of 4-momentum (p). The electron then leaves the interaction vertex with 4-momentum (k'). The energy ν of the virtual photon and the square of the momentum transferred to the hadron Q^2 is large. We have $\nu = k - k' \rightarrow \infty$ (where E is energy of incident electron and E' is energy of scattered electron) and $Q^2 \rightarrow \infty$. While these quantities are kept large, the momentum fraction carried by a parton $x = \frac{Q^2}{M\nu}$ (where M is the mass of the hadron) is kept small (≤ 1). In this limit, the virtual photon interacts directly with a parton. Parton Distribution Functions (PDFs) give the probability that a

parton (quark and gluon) inside a hadron would be carrying a fraction x of the hadron's total longitudinal momentum [Gri04a].

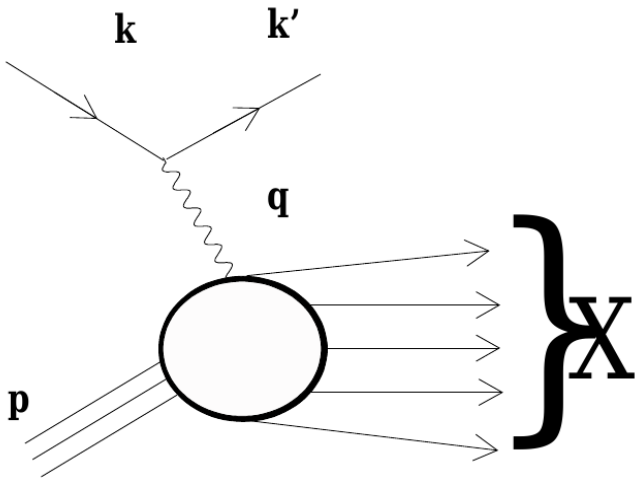

Figure 2.1: Tree diagram of virtual photon interacting with hadron. An incoming electron exchanges a virtual photon with a parton inside the hadron [Cam05b].

Parton distributions are related to a set of functions called structure functions in the perturbative regime of QCD. In this regime, the two most important structure functions F_1 and F_2, are related to the parton distributions for quark q and anti-quark $\bar{q}$ as follows

$$F_1(Q^2, x) = \frac{1}{2} \sum_i e_i^2 (q_i + \bar{q}_i) \tag{2.3}$$

$$F_2(Q^2, x) = \sum_i x e_i^2 (q_i + \bar{q}_i) \tag{2.4}$$

In the parton model, the partons are non-interacting. The parton model was used by Feynman to explain deep inelastic scattering data. The data had confirmed a prediction by James Bjorken that at very high energies, the inelastic structure functions become independent of the resolution of the lepton probe (q^2) and are just functions of x [Gri04a].

Similarly to FFs, PDFs are also very well established and accepted tools to study the structure of nucleons. Both PDFs and FFs contain information about the structure of

hadrons that complement each other. In order to get a clearer picture of the structure of hadrons from FFs and PDFs, both pictures need to be combined. This is done with Generalized Parton Distributions.

2.1.2.3 Generalized Parton Distributions

Generalized parton distributions (GPDs) unify the spatial picture produced by form factors, with the momentum picture produced by parton distributions. In this section, a brief discussion of GPDs will be given.

Recall that the phase space picture from classical mechanics unifies the momentum and position picture of classical systems and provides complete information about the dynamical behaviour of a classical system. GPDs arise from an idea called a Wigner distribution which is a function defined on phase space variables in quantum mechanics [BR05]. Form factors and parton distributions arise as limiting cases of GPDs. The form factors are recovered when the GPDs are projected in the transverse spatial direction and the parton distributions recovered when GPDs are projected in the longitudinal momentum. There are four types of GPDs (see green region of Fig. 2.2 - $H_q(x,\xi,t)$, $E_q(x,\xi,t)$, $\tilde{H}_q(x,\xi,t)$ and $\tilde{E}_q(x,\xi,t)$, where x is the momentum fraction carried by a parton inside the nucleon, ξ is the momentum fraction transferred to a parton by the virtual photon which is exchanged between the parton and the lepton probe and t is the momentum transferred to the hadron.

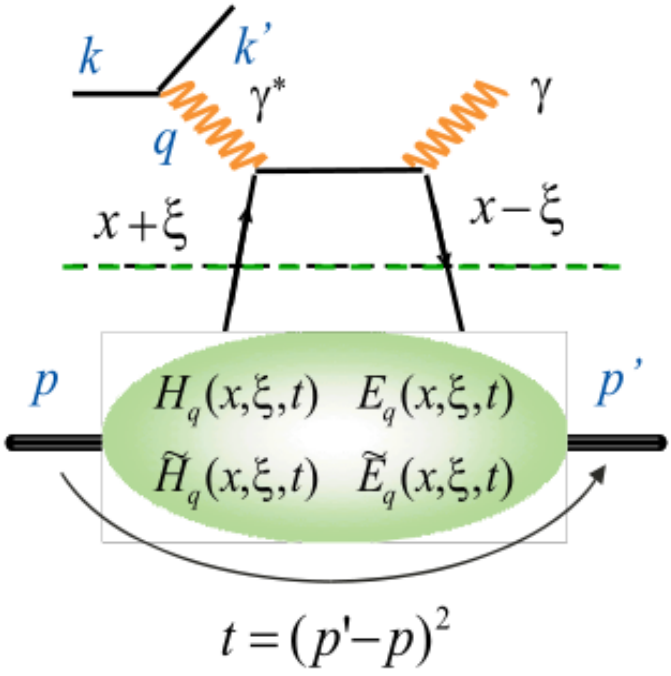

Figure 2.2: Handbag diagram. Electron exchanges virtual photon with a quark and 'knocks' the quark outside the hadron, giving it a momentum fraction of $x + \xi$. The quark then falls back inside the hadron, with a momentum fraction of $x - \xi$, emitting a real photon in the process [eatHADC03].

The GPDs are defined for each quark flavor. For a quark of flavour i, and in the limit of $t \to 0$

$$H^i(x, 0, 0) = q_i(x) \tag{2.5a}$$

$$\tilde{H}^i(x, 0, 0) = \Delta q_i(x) \tag{2.5b}$$

where q_i and Δq_i are the quark and the quark helicity distributions respectively.

In order to recover the form factors from the GPDs, one looks at the first moment of the GPDs [Gui05]

$$\int_{-1}^{1} dx H^i(x,\xi,t) = F_1^i(t), \quad \forall\xi \tag{2.6a}$$

$$\int_{-1}^{1} dx \tilde{H}^i(x,\xi,t) = G_A^i(t), \quad \forall\xi \tag{2.6b}$$

$$\int_{-1}^{1} dx E^i(x,\xi,t) = F_2^i(t,\xi), \quad \forall\xi \tag{2.6c}$$

$$\int_{-1}^{1} dx \tilde{E}^i(x,\xi,t) = G_p^i(t), \quad \forall\xi \tag{2.6d}$$

where $F_1(t)$ and $F_2(t)$ are the Dirac and Pauli form factors respectively (linear combinations of the electric form factor G_E and the magnetic form factor G_M). G_A and G_p are axial and pseudoscalar form factors respectively. One then uses the second moment of the GPDs to recover the total angular momentum of the quarks inside the nucleon via the Ji sum rule [Gui05]

$$\int_{-1}^{1} dx x[H^i(x,\xi,0) + E^i(x,\xi,0)] = \frac{1}{2} J^i, \quad \forall\xi \tag{2.7}$$

where J^i is the total angular momentum of each quark.

GPDs are experimentally accessible via the interference of DVCS with a process called the Bethe-Heitler process (Fig. 2.4) where the real photon of the final state is emitted by the electron and not the hadron. The (5-fold) DVCS cross-section is given by [Cam05a]

$$\frac{d^5\sigma}{dQ^2 dx d\phi_e dt d\phi} = \frac{\alpha^3 xy}{16\pi^2 Q^2 \sqrt{1+4x^2M^2/Q^2}} \left|\frac{\mathcal{T}}{e^3}\right|^2 \tag{2.8}$$

where ϕ_e is the azimuthal angle of the electron scattering plane, ϕ is the angle between the leptonic and hadronic plane (Fig. 2.3). $\mathcal{T}$ is the scattering amplitude which is the superposition of the BH and DVCS amplitudes ($\mathcal{T} = \mathcal{T}_{DVCS} + \mathcal{T}_{BH}$).

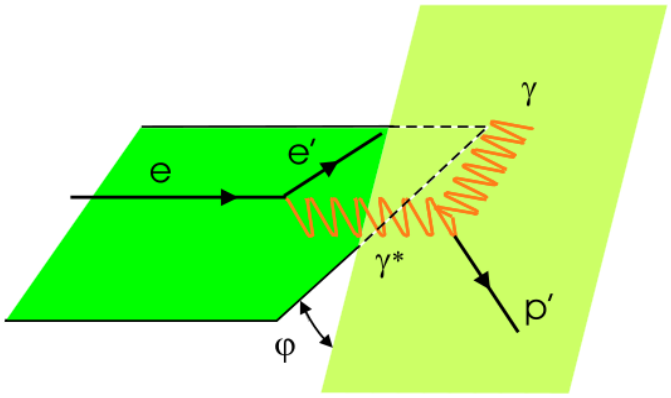

Figure 2.3: Azimuthal angle between hadronic plane and leptonic plane. The electron scatters in one plane (bright green), emitting a virtual photon in the same plane which interacts with the valence quarks of the proton. The proton then recoils in another plane (light green). The proton plane is at an angle relative to the electron plane [Cam05a].

Both the DVCS and BH processes have the same final state, which is why the interference occurs. The interference allows for the simultaneous determination of the real and imaginary parts of the DVCS amplitude and allows for a three dimensional experimental determination of the nucleon degrees of freedom. The DVCS scattering process is

$$\gamma^* p \rightarrow \gamma p, \tag{2.9}$$

where γ^* is a virtual photon and γ is a real photon. Eq. (2.9) is non-unique in that there are other processes (such as the Bethe Heitler) which also have the same interaction (see Fig. 2.4. In Fig. 2.2 (called the handbag diagram), the photon is energetic enough to interact with a single quark directly, giving it a momentum fraction $x + \xi$ with the quark entering a final state with a momentum of $x - \xi$ in the hadron. The hadron then recoils with a momentum of p'. The overall effect amounts to an electron transferring a momentum of t to the hadron.

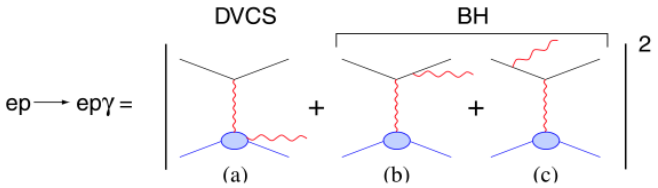

Figure 2.4: Diagram of $ep \rightarrow ep\gamma$ process. The $ep \rightarrow ep\gamma$ process involves two processes that interfere with which other, the Bethe-Heitler process and the DVCS process [Cam05a].

The main aim of the DVCS experiments is to have a high resolution mapping of the spatial and momentum distribution of quarks and gluons in nucleons by studying the interference of the DVCS and BH terms.

3 Goals of DVCS3 and Experimental Setup

In this chapter, the experimental setup that will be used to carry out the third generation DVCS experiment (DVCS3) will be discussed. The discussion will lead into the goal of the DVCS3 experiment and how JLAB will be used to meet this goal.

3.1 Goals of DVCS3

[1]The new DVCS experiment, DVCS3, is an extension of previous DVCS experiments done in Hall A at JLAB. Previous Hall A experiments ([eatHADC00] and [eatHADC03]) measured the absolute cross-sections for $H(e,e'\gamma)p$ (DVCS on proton) and $D(e,e'\gamma)pn$ (DVCS on neutron) at $x = 0.36$. The goal of the new DVCS experiment (DVCS3) is to make measurements of $ep \rightarrow ep\gamma$ cross-sections at a fix x by extracting the angular harmonic terms over a wide range of Q^2. The measurement will serve as a test of the QCD factorization theorem.

The Q^2 dependence of the interference of the imaginary term of the DVCS amplitude with that of the BH term puts a limit on the contribution of higher twist terms (terms which reflect loop contributions) on the extraction of the so called handbag amplitude. Results from [eatHADC00] indicated there was no dependence of twist-2 and twist-3 observables on Q^2 supporting the theoretical prediction that DVCS scaling is foundationally similar to that of DIS scaling[LHAC06]. The work has taken the field closer to proving the dominance of leading twist terms where one is scattering off of a single quark. This is the first time anyone has been this close to proving the leading twist dominance. The work is important in understanding the structure of nucleons in terms of GPDs.

The previous experiments were done in a small range of Q^2 ($< 2.0GeV^2$) as this was the range the available beam energies allowed at the time. In order to complete the proof of the dominance of the leading twist terms, one must expand the Q^2 range. This is now

[1] The discussion (and diagrams) included in this section is based on the proposal for the DVCS3 experiment [LHAC06]

possible with the upgrade of the accelerator such that it has the capability of going from $6GeV$ to $12GeV$ maximum energy. The new experiment will perform a higher precision test of the previous results. This experiment will be done in the kinematic range depicted in Fig. 3.1. The coloured (green, red, blue) shapes represent the beam energies that will be used to probe a given kinematic region. As shown, the experiment will be conducted at three different beam energies (6.6 GeV, 8.8 GeV, 11.0 GeV) with a polarized beam. The cross-section differences ($\sigma^+ - \sigma^-$) and sums ($\sigma^+ + \sigma^-$) will be measured (where σ^+ and σ^- are the cross-sections corresponding to the different helicities).

The exact kinematics, beam current, as well as data rates, the length of time for which beam will be delivered for the experiment are given in Tab. 3.1. In addition, the expected rate of DVCS events and DIS events (where $DVCS \subset DIS$) are given in Tab. 3.1.

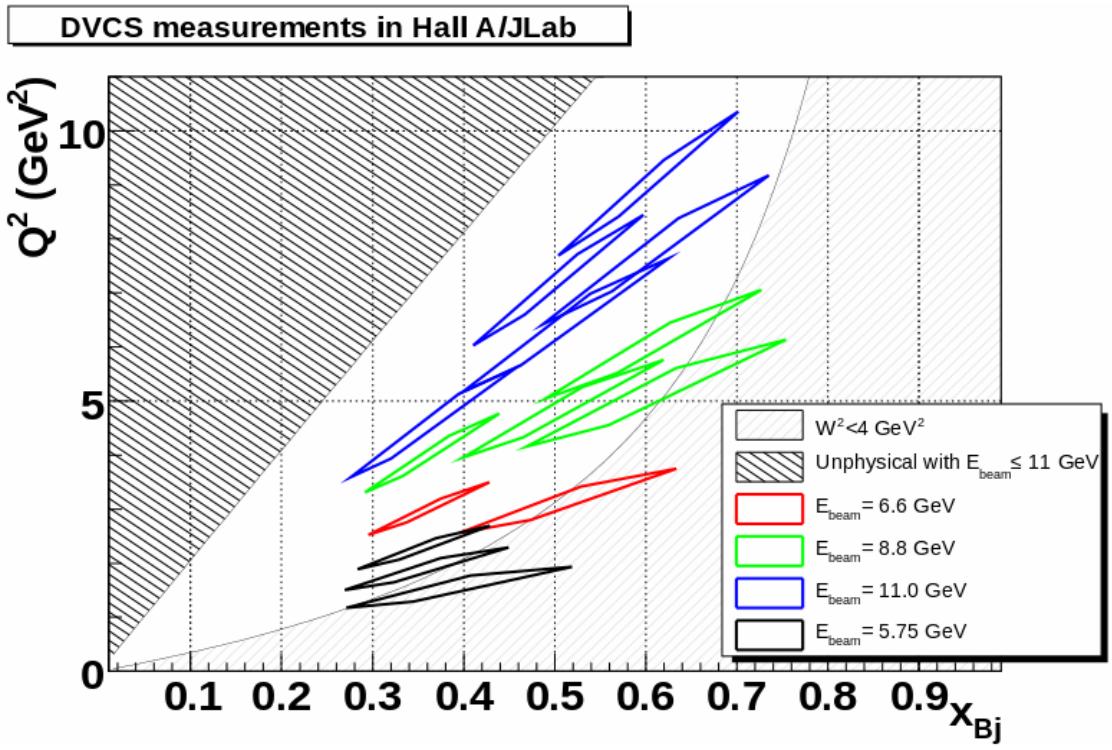

Figure 3.1: Kinematics reach for DVCS3 [eatHADC00].

Q^2 (GeV^2)	k (GeV)	x	$q'(0°)$ (GeV)	D (m)	θ_q (deg)	θ_{calo}^{min} (deg)	I_e (μA)	$\mathcal{L}/10^{37}$ (cm^{-2}/s)	DIS (Hz)	DVCS (Hz)	Time (days)
3.0	6.6	0.36	4.35	1.5	11.7	7.1	4.7	1.9	100	0.3	3
4.0	8.8	0.36	5.83	2.0	10.3	7.0	8.3	3.3	170	0.43	2
4.55	11.0	0.36	6.65	2.5	10.8	7.0	13.0	5.2	500	1.2	1
3.1	6.6	0.5	3.11	1.5	18.5	11.0	4.7	1.9	190	0.2	5
4.8	8.8	0.5	4.91	2.0	14.5	8.9	8.3	3.3	120	0.2	4
6.3	11.0	0.5	6.5	2.5	12.4	7.9	13.0	5.2	130	0.26	4
7.2	11.0	0.5	7.46	2.5	10.2	7.0	13.0	5.2	50	0.13	7
5.1	8.8	0.6	4.18	1.5	17.8	10.4	4.7	1.9	50	0.07	13
6.0	8.8	0.6	4.97	2.0	14.8	9.2	8.3	3.3	32	0.05	16
7.7	11.0	0.6	6.47	2.5	13.1	8.6	13.0	5.2	39	0.08	13
9.0	11.0	0.6	7.62	3.0	10.2	7.3	19.0	7.4	17	0.05	20

Table 3.1: Kinematics for the DVCS3 Hall A experiment.

3.2 Method

In doing this experiment, the $H(e,e'\gamma)X$ and $H(e,e'\pi^0)X'$ reactions are measured by detecting a scattered electron in the left HRS and emitted γ-rays in a 13×16 PbF_2 calorimeter. The electrons will be detected in a High Resolution Spectrometer whose trigger forms from a coincidence signal in the s2 scintillator plane and Cerenkov detector. The 208 channels of the PbF_2 calorimeter will be connected to the inputs of 13 analogue ring sampler (ARS) boards (each with 16 channels) capable of digitizing events at a rate of 1 GHz. Each channel of the ARS will store 128 analog samples at 1 ns per sample. The analog signals are serially digitized within 128μs.

One must do an offline analysis in order to identify the $H(e,e'\gamma)p$ and $H(e,e'\pi^0)p$ reactions out of the $H(e,e'\gamma)X$ by doing the missing mass calculations (Fig. 3.2). One must remove the π^0 events, which may sometimes appear as DVCS events in the calorimeter. This occurs when one of the photons from the π^0 decay misses the calorimeter. The missing mass of the one photon π^0 decay events is done with the assistance of Monte-Carlo simulations using the events where two photons were detected (from two photon π^0 decay events) results from the particular experiment which are then used to estimate the case where only one of the photons from the π^0 decay is detected. One then subtracts these events from the raw data.

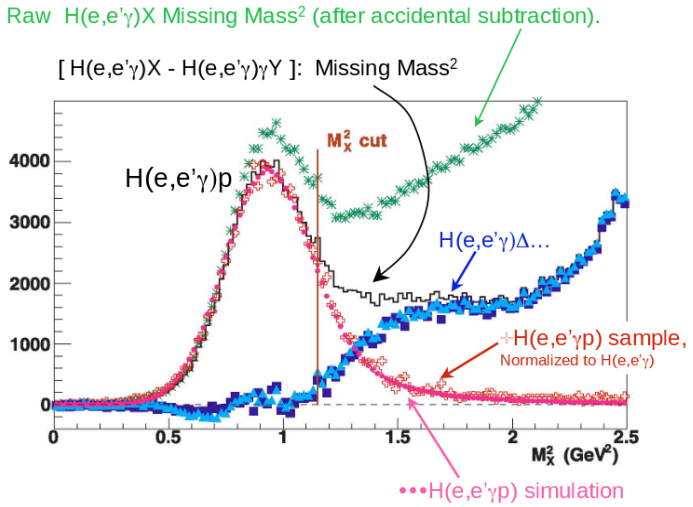

Figure 3.2: Missing mass for identification of $ep \rightarrow ep\gamma$ events[HW07]. This identification involves first eliminating processes that are not actually of the type $ep \rightarrow e'p\gamma$ out of $ep \rightarrow e'\gamma X$ measured by the data acquisition system. The events of type $H(e,e'\gamma)X$ which are identified by the coincidence between the HRS and the calorimeter are shown in green. Next, one removes the π^0 events ($H(e,e'p)X - H(e,e'\gamma)\gamma Y$), resulting in the black line. A cut is placed where the events that involve the production of other pion events alongside a delta (blue points) are negligible. Finally, one is left with the $ep \rightarrow ep\gamma$ events (red points). In a previous experiment, the red points were obtained by detection of the proton recoil (a step which was later found to be unnecessary).

3.3 Experimental Setup

3.3.1 JLab

JLAB is a US government research facility whose main focus is the study of the structure of nuclear matter. The reasons why this facility was chosen to do the DVCS experiments was because it has

1. High duty factor - This is the ratio of the pulse time width to the time between the pulses. The DVCS experiment involves making a coincidence measurement between a photon and an electron. Coincidence measurements are improved upon by having a large duty factor. This is because accidental events and real events compete with each other. With a high duty factor, the number of accidental events is decreased. At JLab, the high duty factor (of 99%) is obtained by spreading the electrons of the beam out in time (making what is called a continuous beam).

2. Polarized beam

3. Good beam energy - The facility's beam energy of 12 GeV makes it possible to perform the experiment at a relatively large Q^2 range ($> 2GeV^2$).

The facility consists of two superconducting linear accelerators (LINACs) linked by five arcs as depicted in Fig. 3.3.

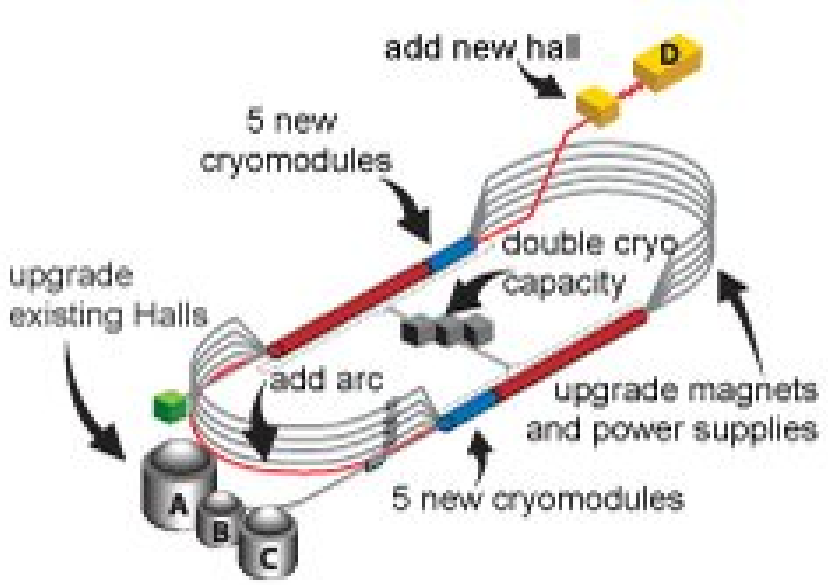

Figure 3.3: Setup of Continuous Electron Beam Facility (CEBAF) at JLAB [JLa13]. A single beam is injected into the four halls.

A beam of electrons travel from one LINAC to the other and is circulated at the required amount of times needed to bring it at a particular energy. The facility has just been upgraded to double its maximum possible beam energy from 6 GeV to 12 GeV. From the arcs, the beam is injected into all four halls (Hall A, B, C and D (newest)). These arcs allow for the delivery of 1 to 5 times the energy from the LINAC into the halls. The facility uses superconducting radio frequency technology - using liquid helium to cool niobium to around 4 K. The accelerator is 8 m below the earth's surface.

3.3.2 Hall A for DVCS

The new DVCS experiment is to take place in one of the four halls at JLab (Hall A). The main equipment of Hall A are two identical 4 GeV/c High Resolution Spectrometers (see Fig. 3.4). These spectrometers have a momentum resolution of 2×10^{-4}. One of these spectrometers (left spectrometer) will be used to detect electrons from an incoming beam

of energy 12 GeV (or less). The left HRS detector package (electron arm in Fig. 3.4) consists of two scintillator planes -S1 and S2 - which are 2m apart. The planes are made of six and sixteen plastic scintillators which overlap.

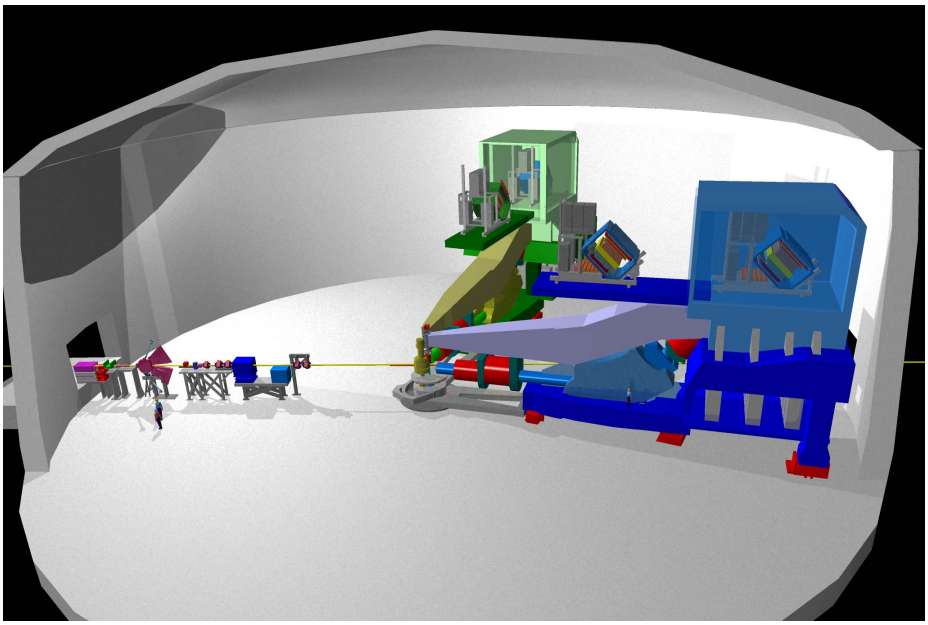

Figure 3.4: Hall A setup involves two High Resolution Spectrometers, the left spectrometer is reserved for electrons, whereas the right spectrometer is for hadrons [JLa].

Two Photo Multiplier Tubes (PMTs) collect signals from each scintillator. In the experiment, negative pions are produced in the background. As negative pions can be mistaken for electrons, there needs to be some means to identify them so that the real $H(e, e'\gamma)X$ events can be identified out of the background. This is done with a gaseous CO_2 Cerenkov detector. The particles are tracked using Vertical Drift Chambers (VDC).

The hall's luminosity reach of $10^{38}\ cm^{-2}s^{-1}$ allows it to be capable of carrying out DVCS experiments. This luminosity is important as a certain number of days are assigned for the completion of the experiment. At this luminosity, enough data that will meet the goals of the experiment will be taken within the assigned number of days.

3.3.3 Beamline

The hall has the following equipment in the path of the beam (beamline):

1. Beam position monitors - Four antennas placed around the beam that provide measurements on the beam's position.

2. Beam current monitors - Provide measurements of the beam current.

In the path of the beam is the target chamber which will contain 15 cm of LH_2. The electron beam will travel along the path indicated by the red line in Fig. 3.4. The beam will collide with the liquid hydrogen target and the electrons will be scattered as depicted in Fig. 3.5. The electrons will be detected in the left spectrometer and the photons detected by a 13×16 PbF_2 calorimeter which will be placed at angles as small as (7°) from the beam as shown in Fig. 3.5.

3.3.4 Calorimeter Properties

The properties of the calorimeter are given in Fig. 3.3.4. The Moliere radius (the radius through which a shower of particles span when a photon hits the calorimeter block) is such that if a photon hits the center of a PbF_2 block, then most of the energy will be deposited in that one block. The calorimeter was designed having the following in mind

- PbF_2 is a pure Cerenkov crystal medium that is radiation hard.

- Low sensitivity to low energy nuclear particles allowing the use of 1 GHz Analog Ring Samplers for the minimization of pileup.

- Small Moliere radius allowing for the separation of closely spaced showers coming from π^0 decay and minimizes shower leakage at the boundaries.

- A short radiation length which minimizes fluctuations in light collections.

Physical Property	Values
Density	$7.77 g/cm^3$
Radiation Length	$0.93 cm$
Moliere Radius	$2.20 cm$
Index of Refraction	2.05 ($\lambda = 180 nm$) 1.82 ($\lambda = 400 nm$)

Table 3.2: DVCS Calorimeter properties.

The calorimeter will be placed at a closest distance of 1.5m and a farthest distance of 3.0m from the target. The scattering chamber depicted has a 63cm radius and has a 1cm thick Al wall. There will be a beam pipe of 6° measured on left and right relative to the horizontal depicted in Fig. 3.5 and will be 6m long.

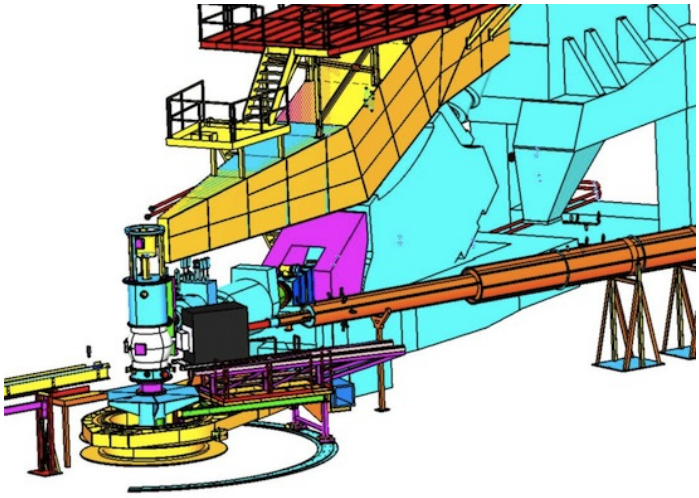

Figure 3.5: Setup for DVCS3 [Roc14]. The Calorimeter (black box) will be placed at small angles (about 7°) relative to the beam line. This is because the DVCS process involves forward scattering.

The calorimeter and the HRS will be ‘linked’ by the trigger module which will select events where a photon arrives in the calorimeter in coincidence with an electron in the left HRS. The entire collection, transfer and storage of the data is ‘overseen’ by the data acquisition system.

3.3.5 Systematic Error predictions

For the experiment, there are some sources of systematic errors to take into consideration. They are listed in Tab. 3.3.5.

Type		Relative errors (%) proposed
Luminosity	Target length and beam charge	1
HRS-Calorimeter	Drift chamber multi-tracks	1.0
	Acceptance	2.0
	Trigger dead-time	0.1
DVCS Selection	π^0 subtraction	1.0
	e(p,e’γ)πN contamination	3.0
	radiative corrections	1.0
Total Cross-section sum		4.1
Beam	Polarization $\Delta P/P$	1.0
Total Cross-section difference		4.2

Table 3.3: Contributors to DVCS systematic errors.

The work for this thesis will contribute in meeting the goal of the systematic error coming from dead-time. How well the dead-time for the whole data acquisition system is

known will have a small contribution to the systematic error as the dead-time will be kept as small as possible.

4 Introduction to Data Acquisition System

4.1 General Information

Data acquisition is the process of measuring physical data (e.g. sound) with a computer [DPE13]. There are three main parts:

1. Sensor (Detector)
2. DAQ Hardware (front-end electronics)
3. DAQ Software (on computer)

In Fig. 4.1, we have the sensor which produces electrical signals from the analog input (coming from signals generated by particle events seen by detectors) which is then sampled using analog-to-digital converters and eventually stored.

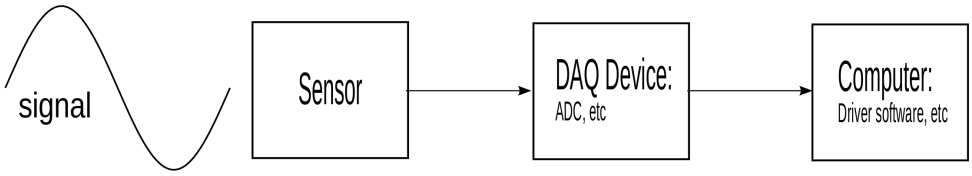

Figure 4.1: Analog signal is read and converted to digital signal and sent to CPU.

The entire process, from start to conclusion, takes some time and involves the following stages (embedded in Fig. 4.1):

1. Triggering-*Choosing events of interest. If an event considered as valid is detected, the signal is measured by the ADC.*
2. Readout-*Digitization of signals from detector(s). This is done by the ADCs.*
3. Transfer of data -*After the events of interest are digitized, they are transferred from various read-out devices to a central CPU.*

4. Data storage-*Data is saved to the computer harddrive, a process which usually takes a lot of time.*

During this time (dead-time), the DAQ is unable to digitize and transfer anymore events. How long this lasts will actually affect how well the cross-section is measured in the experiment. The smaller the dead-time, the better the cross-section will be measured. It is therefore very important to have a DAQ which has this dead-time being as small as possible. In order to have as small a dead-time as possible, one has to have a system specifically for the experiment, that performs the stages from trigger to storage as quickly and as efficiently as possible. The importance of the above stages merit further discussion, particularly for the case of DVCS and this will be done in the sections to follow.

4.2 Triggering

The task of selecting out the reactions of interest from competing reactions that occur simultaneously is a very important part of data acquisition [Leo94]. This process is called triggering and the electronic logic for the selections is called a trigger. This is done by imposing some criteria that is characteristic of the reaction of interest. When events satisfy the criteria, further electronic operations are activated, such as digitization for example [Leo94]. Possible criteria may be, the energy of outgoing particles, the coincidence of two or more outgoing particles within two or more detectors. Triggering is important as it helps to reduce the rate of incoming events and thus help reduce dead-time of the experiment.

In the DVCS experiment, when an electron arrives in the high resolution spectrometer (HRS), a photon is expected to arrive in the calorimeter right after. Here, right after means within a defined time period set by hand (the coincidence time). Once it is determined that the arrival time of the photon in the calorimeter relative to that of the electron in the HRS is within the coincidence time, the energy deposited by the photon in

four adjacent calorimeter blocks where the photon arrived are summed and this sum is compared to a threshold value (about 2.5 GeV). If the sum is at or above this threshold, the event is digitized. There is more to this and further details will be discussed in chapter 5.

In order for the DAQ to perform its various operations, it is important to have the appropriate hardware and software. In the next section, the hardware will be described.

4.3 Front-end electronics

Data acquisition hardware provides the bridge between the analog and the digital world. It consists of electronics that have to do with the readout and transfer of data. The DVCS experiment uses devices known as analog ring samplers (ARS) to sample incoming signals which are then digitized by an ADC if instructed to do so. The samplers are placed in two crates, each of which have a single computer that communicate with the boards and sends information to the central computer via a network. This setup allows for parallel processing of the modules, optimizing the data transfer rate and hence reducing dead-time. The status of the ARS (i.e. whether or not they are ready to take data) is communicated to a component called a trigger supervisor (TS). The TS inhibits any trigger while the data is being processed.

The stage where the analog signals are converted to digital signals is extremely important as without the signal in digital form, one could not make the measurements of the observables needed to do the physics. The process involves a finite sampling of an incoming analog signal, converting the signal from continuous to discrete form. In nuclear/particle physics experiments, this signal is in the form of a pulse. The polarity, shape or the amplitude of the pulse contains information about the process that generated the pulse.

The first stage in analog-to-digital conversion involves discretely sampling the continuous signal - the information is thus of a quantized nature and thus has a finite

number of states (where the analog signal had infinitely many states) [Leo94]. In most cases in nuclear physics, one has only two digital states; yes (1) or no (0). The fact that there are only two digital states means that the process of analog-to-digital conversion loses some information about the analog signal. In addition, there is limited information carrying capability of a single logic signal. This limiting capability of the logic signal is reduced by using multiple logic signals (increasing the resolution of the ADC) in order to represent the analog signal in numerical form. As a result, a single analog signal would be represented by a string of binary numbers which may either be transmitted in series, or in parallel [Leo94]. There are different kinds of ADCs; fast ADC (e.g. the analog ring samplers in DVCS), time-to-digital converters (TDC), etc. In the simplest example of an ADC, where there is a 1-bit output, a discriminator is used to check if the voltage corresponds to a signal that is considered valid before the signal is digitized [Leo94]. In this case, the ADC outputs 1 whenever the signal is valid and 0 if the signal is not valid. In this case, the discriminator is the electronic component that practically selects the events of interest to a particular experiment. A device known as a counter (or scaler) is used to register the valid event.

In a more complex system, where the trigger replaces the discriminator. The digitizer would be an n-bit ADC, where n is the resolution of the ADC. There are 2^n possible representations of the n-bit ADC. In Fig. 4.2, there is an 8-bit output. For this ADC, the digital output goes from 0 to $2^8 - 1 = 255$.

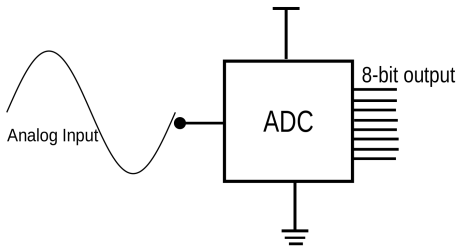

Figure 4.2: Analog signal converted to discrete 8-bit signal.

A particular ADC would be designed to accept input voltages within a specific range. The number of possible binary representations is dependent on the number of bits the ADC is made to output. The total number of representations divides this larger acceptance range into smaller voltage ranges that may be of equal length (subintervals). Each binary representation represents each subinterval and as one transitions from one interval to the next, there is some voltage threshold present for each transition. There are $2^n - 1$ such transitions for an n-bit system hence why the ADC outputs values from 0 to $2^n - 1$.

Example 4.3.1. *Suppose we had a 2-bit ADC with an acceptance range of* $0 - 4V$*. Since this is a* 2*-bit system, there are* 2^2 *binary representations (right most image in Fig. 4.3). This represents* $2^2 - 1$ *voltage thresholds (right most image in Fig. 4.3). The voltage threshold may occur at multiples of*

$$V_T = \frac{4.0V - 0.0V}{2^2}$$
$$= 1.0V$$

where V_T *is the threshold voltage.*

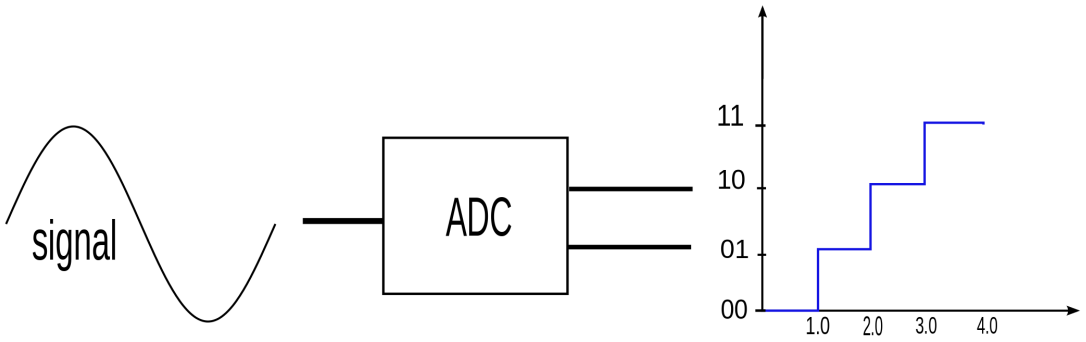

Figure 4.3: 2-bit system. As this 2-bit ADC digitize the data, different voltage thresholds are surpassed to move to the next bit level.

This is shown in Fig. 4.3 where we have a 2*-bit ADC converting an incoming analog signal to a digital form.*

4.4 The DVCS Analog Ring Sampler

The analog ring sampler consists of 128 capacitor cells arranged in a ring formation. Each cell is charged when they are connected to the signal (i.e. they are in the track state) and are then isolated after some time (i.e. placed in the hold state). The number of cells in this state (hold state) is constant. A STOP signal and a VALID signal controls the sampling and digitization process in the following way [Cam05a]:

1. The overwriting of each cell is stopped on the command of the STOP signal.

2. After each STOP signal, the cells in the track state that are filled are then switched to the hold state. During this time, the cells that were already in the hold state remain so.

3. Sampling is completely stopped when all the cells are in the hold state.

4. If a signal VALID is then sent by the trigger module, the signals stored in the capacitors is then digitized using ADCs and eventually sent for storage.

This process is reflected in Fig. 5.1.

The digitized data can be used to resolve cases where a single event's energy may be incorrectly computed as the sum of two photons that the calorimeter is unable to distinguish. This happens when the photons of the two events are deposited too closely (in space) in the calorimeter. This leads to what is called an event pile-up. An event pile-up would look like that in Fig. 4.4.

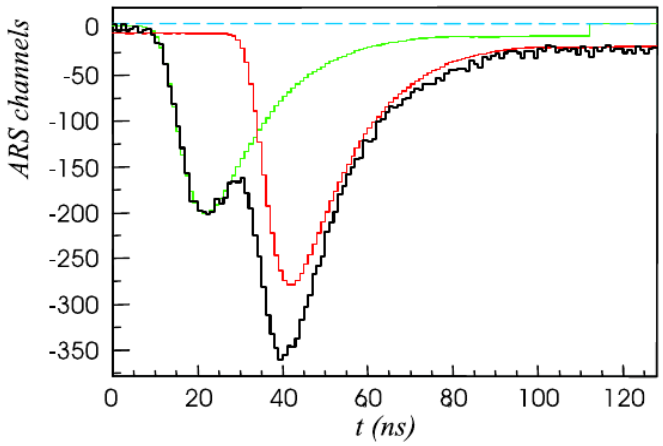

Figure 4.4: Pile-up of events in the calorimeter [Cam05a].

It is important to be able to identify and remove these events for they may be misidentified as DVCS events. In order to handle this in the DVCS experiment in Hall A at JLab, the ARSs sample at a rate of 1 GHz.

The ARSs and all the hardware used are controlled by different types of software which will now be discussed in the next section.

4.5 DAQ Software

The DAQ software is an important aspect of the DAQ. It allows communication between the main computer recording data and the many pieces of hardware. There are two kinds of software important for the DAQ [TM02]:

- Application software - allows one to control dead-time as well as the input/output of the different CPUs.
- Driver software - used to control the DAQ hardware.

There is relationship between the user, DAQ application software, DAQ driver software and hardware. This is shown in Fig. 4.5. The user sends instructions via the application software, which may be in the form of a graphical user interface. In DVCS (or other

experiments), the user has the option to choose to start and to stop collecting data using the application software, CEBAF Online Data Acquisition (CODA). Meanwhile, this software would provide the user with information such as whether or not a CPU controlling a set of ARSs is receiving power for example. It may also give the user other information such as when there is no triggering of the ARSs. The driver software exchanges information with the application software. The DVCS trigger uses Field Programmable Gate Arrays (FPGAs) which have special codes written for them that allow these chips to collect data from the ADCs (hardware) to be assembled and dumped into a data file. The FPGA codes are driver software for the trigger.

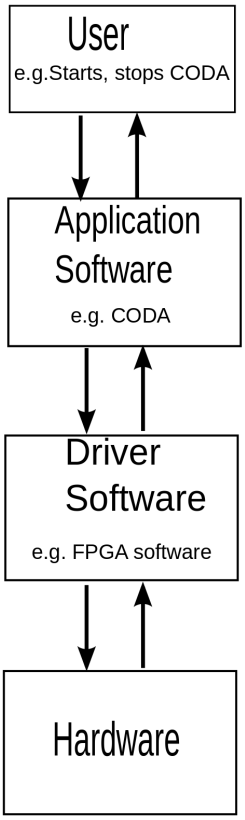

Figure 4.5: Relationship between user, DAQ application software, DAQ driver software and DAQ hardware. The arrows show the flow of information from one place to the other.

The complete operation of the DAQ requires that information flows properly in each of the cases depicted in Fig. 4.5. In the next few subsections, the driver software and application software will be discussed.

4.5.1 The Driver Software

The driver software (Fig. 4.5) is the software used to control the DAQ hardware [TM02]. For the new DVCS experiment, the software on each of the 13 ARS boards that tells the board it is being instructed to sample a signal is an example of a driver software. Some of the purpose of the driver software is to [TM02]

- Get data
- Monitor the experiment
- Integrate the DAQ hardware with the computer

The next thing that one needs is for a human to be able to control the DAQ to perform useful tasks (such as starting and stopping the data collection process, configure the experiment). This is done with the application software. The DVCS experiment has a bridge between the driver software for the ARS boards and the application software (CODA). This bridge is a read-out list which contains information about the number of ARS boards and how data is transferred from trigger to conclusion (which is done with certain data transfer protocols).

4.5.2 The Application Software

The application software (second from top of Fig. 4.5) is a front end to the driver software that allows one to

- Manage the trigger and the dead-time
- Manage input/output with multiple CPUs that interface

just to name a few. An example of an application software is the one used at Jefferson Lab called the CEBAF Online Data Acquisition (CODA). It was designed for the three experimental halls at Jefferson lab. In CODA, one can setup different configurations for experimental runs. This is shown in Fig. 4.6.

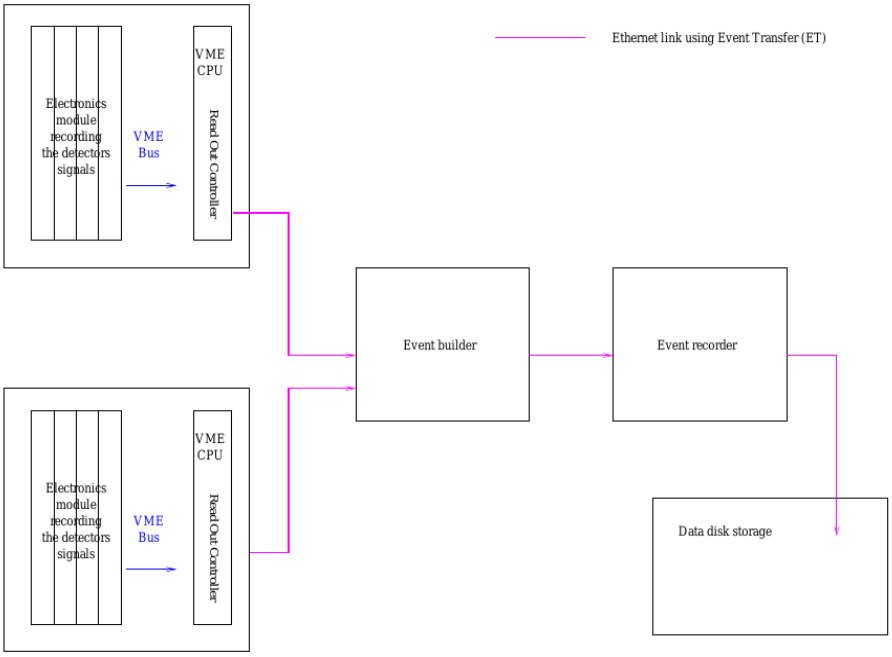

Figure 4.6: A typical CODA configuration [Cam05b].

There are multiple components to CODA. They are [Cam05b]

- The rcserver which contains different experimental configurations and checks the status of the components of a configuration. The GUI component of the rcserver (Run Control) is used to control the DAQ.

- A database (MiniSQL)which holds information such as the run configurations and detailed information (such as computers on which the configuration runs, etc) about these configurations.

- Programs which control the read-out from the detectors. These programs are called Readout Controllers (ROCs) and are ran on VME CPUs which reads out Analog Ring Sampler modules (ARS) which are responsible for sampling and digitizing the incoming signals [Cam05a]. The read-out lists are then provided to the ROCs to extract data from the ARS modules.

- The Event Builder (EB) collects the data from the ROCs and organize them to build events.

- Then the Event Recorder (ER) writes the events to a storage disk.

- In each case, the data is transferred from one component to the next using an Event Transfer (ET) library.

Data acquisition is an essential part of any nuclear and particle physics experiment. For this reason, one must be careful to check that the DAQ is working the best that it possibly can so as to help allow the experiment to be done smoothly. In the next chapter (chapter 5), work on the trigger system for the upcoming DVCS experiment in Hall A at Jefferson Lab will be discussed.

5 DVCS3 Trigger System and Testing Results

The triggering system for DVCS is responsible for selection of events of the type where an electron scattered in the reaction

$$e^- + p^+ \rightarrow e^- + \gamma + X \tag{5.1}$$

is detected in a high resolution spectrometer (HRS). After an electron is detected in the HRS, a logic system then instructs the computers to scan the calorimeter blocks for photons above a 1.5 GeV threshold. If it finds such a photon, then the event is recorded. The event is then read and the data transferred to storage tapes for analysis.

In this chapter, work that has been done on the trigger system for the preparation of the upcoming DVCS experiment in Hall A at JLab will be explained in detail. The trigger was designed, built and tested in France by the Engineer Magali Magne. Magali's testing did not simulate the realistic conditions in which the trigger will be in at the lab. As a result, further testing needed to be done at JLab in order to do this. The trigger arrived at JLab in September 2013. The work done for this thesis began in January 2014 and involves testing the trigger to ensure that it is performing as expected for the upcoming experiment in conditions as realistic as possible. Initially, much of the testing was to check the validity of the ADC readout. For about 4.5 months, the readout had issues (details which will be discussed). Once those issues were resolved, basic bench testing was done to see what else remained to be fixed. These were done in the DAQ and Electronics labs at JLab. The next step was to take it to the testlab and connect the trigger to the calorimeter to do LED and cosmic tests. Then, the ARS was connected to the trigger in an ARS and trigger configuration. The final testing will involve setup in the hall where the experiment will be carried out. It is an ongoing project until the experiment begins in October 2014. The aim of this chapter is to describe the current state of the device since the testing began. Some of the results presented (in particular, those on the

linearity of the ADCs and the validity of the data) were completed in time for an electronics review which was held on May 20, 2014. The remaining results were obtained in time for the deadline (July 25, 2014) to get the trigger to be functional for the experiment. The final testing starts in the first week of August 2014.

5.1 Goal and Design

The overall goal of the new trigger design is to reduce the dead-time of the data acquisition system. Without a trigger, the ARSs are read in 128μs. With a lot of events, this will add up to a very long time. With a trigger however, only events that satisfy an electron in the left HRS forming a coincidence with a photon of energy above 1.5 GeV in the calorimeter will be taken and if such an event is not present, the ARSs will be cleared in 500ns (less than half the time it takes to read an ARS, see Fig. 5.1).

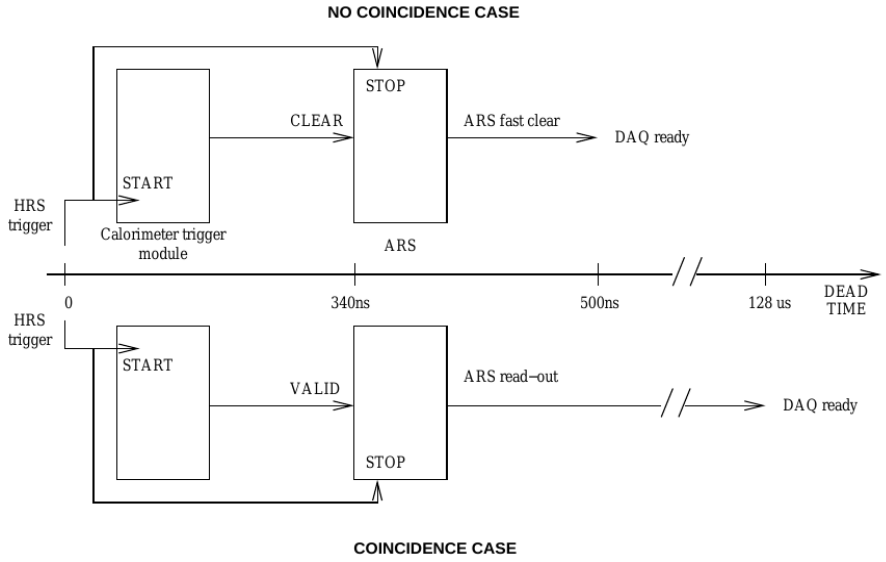

Figure 5.1: DVCS trigger logic[Cam05a]. The DVCS trigger logic involves first waiting for the HRS to stop all ARS and start the trigger module whenever an electron arrives in the HRS. This process takes 340 ns. If no coincidence PMT signal is found above threshold (no coincidence case), then no ARS will be read and the system is cleared in 500 ns. When a coincidence PMT signal is found above threshold (coincidence case), the ARS are read and the whole read-out process takes 128μs (which means that the DAQ is busy during this time).

Reducing the dead-time will allow measurements of the cross-section down to 4% (an improvement to the 5% of the E00-110 experiment done previously). Typically, when a photon gets into the calorimeter, it deposits its energy to multiple blocks. The calorimeter is designed so that the energy will be deposited in a maximum of four blocks. This is done by designing each block in such a way that if a photon hits the center of the block, most of the energy would be deposited in that one block. The photon's energy is obtained by summing the energy deposited by the photon in each of the four blocks. In general, the algorithm works as follows:

1. After an electron is detected in the HRS, sum the channels corresponding to four adjacent calorimeter blocks. There are 180 such groups of four blocks.

2. Check if the sum of the signals correspond to a signal that is equivalent to an energy of 1.5 GeV. This is done by comparing all the quadrature sums.

3. If the sum corresponds to such a signal, read all the blocks.

The calorimeter is a 13×16 calorimeter with a compatible 208 channel trigger module (Fig. 5.2) that uses Field Programmable Gate Arrays (FPGAs) - special computer chips that can be reprogrammed for different use if needs be.

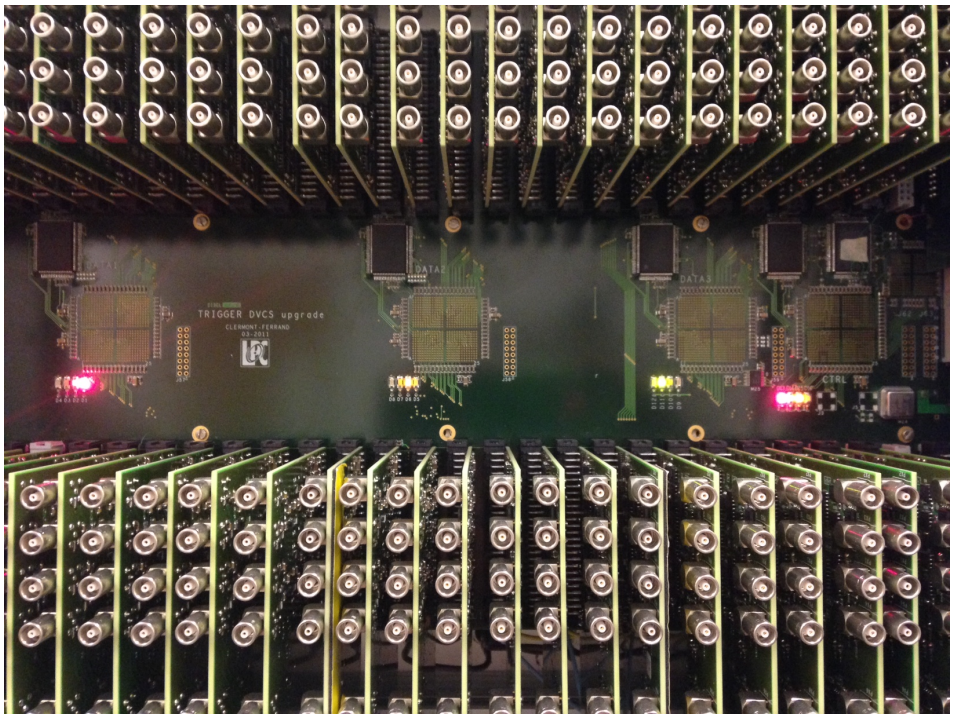

Figure 5.2: Trigger with FPGAs inside. Notice the five black chips at the top, these are the FPGAs. From left to right, there are the first three FPGAs which collect data from the channels. The remaining two FPGAs on the far right are the ones that make the logic decisions.

Fig. 5.3 shows how the trigger will work in the overall setup. When an electron arrives in the HRS, a signal is generated in the s2m and Cerenkov 250 ns after an interaction occurs. A gate is then generated in the trigger 305 ns after the vertex. During this time, a busy signal is generated to prevent any more triggers from being generated. In addition, an ARS stop signal lasting 510 ns is generated and the trigger is instructed to scan all possible combinations of four adjacent blocks (180 such combinations) in the calorimeter and compare the sum of the signal in these four blocks to a set threshold. One may also do a force validation, where the trigger is forced to accept an event. This can be done while taking cosmics or HRS singles. A $500ns$ delay is introduced for this to ensure time to generate a coincidence with a signal from the calorimeter. The signal from the calorimeter takes about $355ns$ to travel to the trigger module. If a valid event is found, a

valid signal is generated and the ARSs are read within 128μs (notice the 128μs gate in Fig. 5.3).

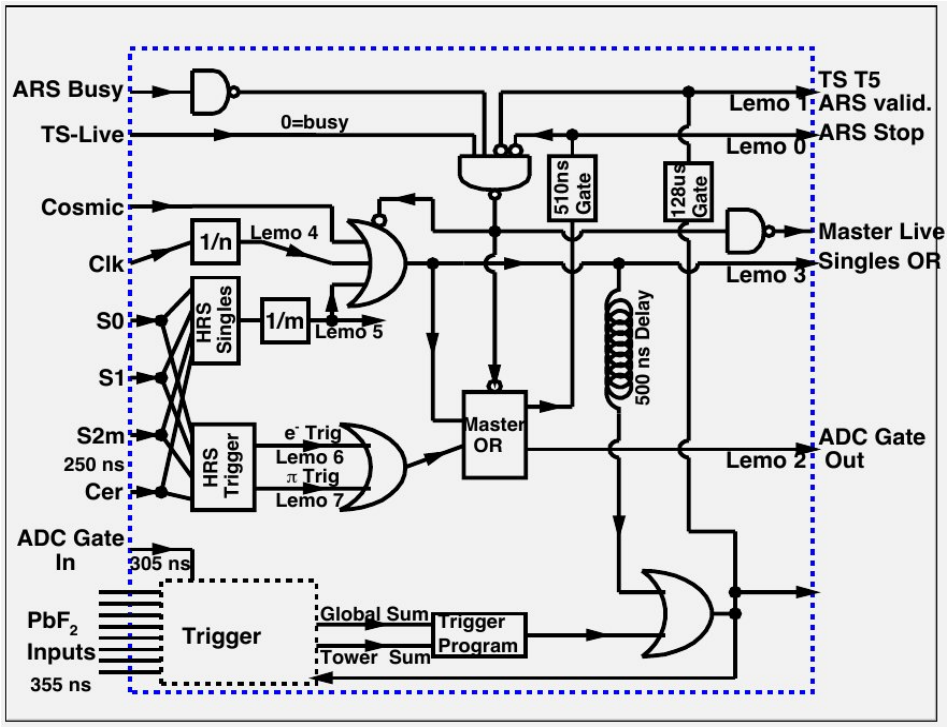

Figure 5.3: Logic diagram of expected behaviour of trigger in the DVCS3 experiment. The trigger logic incorporates momentum information for the electron in the HRS and information about the photon energy in the calorimeter.

With the experiment aiming to measure cross-section sums and differences, uncertainty in the dead-time has a direct impact on the uncertainty of these measurements. In the 2004 and 2010 experiments, the data rate and dead-time were high which required an accurate determination of the dead-time. The uncertainty in the dead-time is proportional to the dead-time (which is in turn proportional to the data rate). In the new experiment, the aim is to reduce the data rate (thus reducing the dead-time) in order to reduce the uncertainty in the dead-time. The new trigger is designed to improve on the dead-time of the data acquisition system in order to help meet the 4% goal in the

systematic uncertainty. The DVCS trigger selects $e\gamma$ events out of a diverse background of DIS events. There are five FPGAs inside the module as shown in Fig. 5.2 that allows the trigger to reduce dead-time. In order to do this, a certain set of ADCs are assigned, one set to each of three FPGAs (see Fig. 5.4). The FPGAs are responsible for summing of four adjacent blocks of the calorimeter. The testing and performance of this new trigger will now be described.

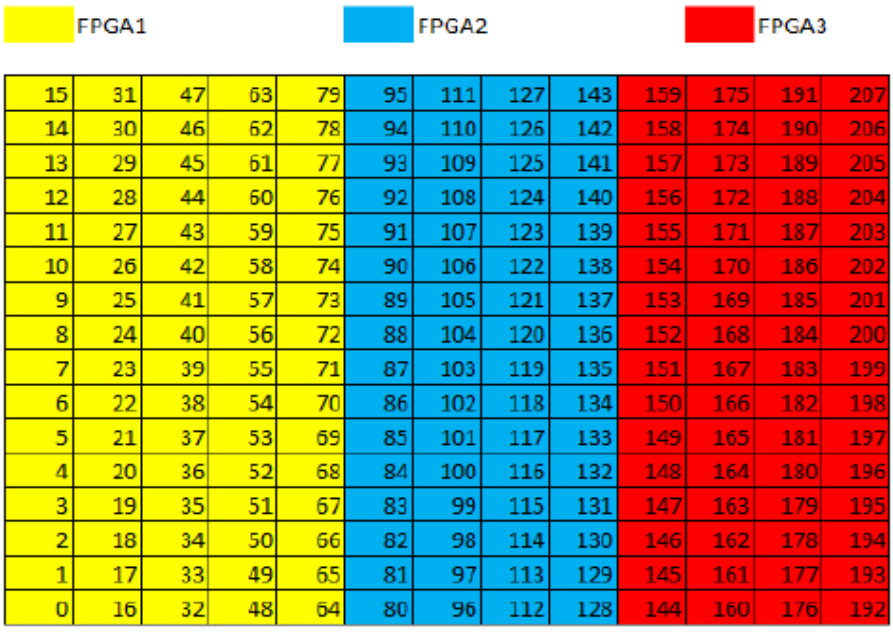

Figure 5.4: Trigger FPGAs and their ADC assignments. The trigger for the upcoming DVCS experiment has five FPGA computer chips (two of which are not shown here) which control the operation of the trigger.

5.2 Expected Behaviour

On arrival at JLab from Clermont-Ferrand, France, the trigger had to be tested to ensure that it is performing as expected. Much of this testing involves constant communication with the Engineer who designed the device in France. Although testing is still being done, some work, which has been done by the author, will be presented.

The data from the trigger takes a specific format where information about counters and the ADCs are stored. The basic format is shown in Tab. 5.1.

Word Number	Word	Description
1	0xaaaaaaaa	This is the header word. Signifies the beginning of the data.
2-28	Counters	These count the number of events when triggering from a specific input.
29	Cluster Found	This indicates if a cluster sum meets the threshold set.
30-33	0x00000000	These are just constant words in the buffer.
34-105	ADC data	These are 32 bit words that store the values of a pair of ADCs.
106-113	0x00000000	These are constant words in the buffer.
114-145	ADC data	These are the remaining 32 bit words that store the values of a pair of ADCs.
146-153	0x00000000	constant words.

Table 5.1: Output of the DVCS trigger module.

The following is the expectation of how the trigger is supposed to behave:

- Should be compatible with block transfer mode - a form of data transfer which involves clumping data in blocks before transferring it. This mode is a relatively faster way of transferring data.
- Integrity of data - The data is checked to make sure that it corresponds with the structure depicted in Tab. 5.1.

- The value of the ADC when it digitizes an event as a function of the input signal to the ADC, is supposed to be linear.
- The event counters (components of the electronics that increment based on the number of events) are supposed to increment by one.
- The trigger is supposed to correctly sum the values of the ADCs both as a cluster of four (for all possible combinations of four) as well as globally.
- The trigger should be able to correctly identify events where a sum of four clusters exceed a given threshold.

The aim of the work for this thesis, was to check that all of the items on the above list are true.

5.3 Testing Procedure and Results

There were two stages to the testing. The first was basic and involved using a deterministic pusler to send pulses at equal intervals of time to the inputs. The rate of the pulse could be adjusted as desired. The maximum rate used was 6kHz as it is not expected that the data rate in the actual experiment will exceed this value. This stage was used to do basic testing of all the items on the above list. The second stage involved testing using cosmic rays which involved connecting the trigger to the calorimeter. This provided a simulation of random (instead of deterministic) events. This is important, for the events in the actual experiment will be random. In addition, these tests allowed investigation of the calorimeter blocks to ensure that they are sensitive to incoming particles.

5.3.1 Trigger output timing signals

The output timing signals of the trigger module were checked with the assistance of Paul King to see if they are as depicted in Fig. 5.3. The timing information was obtained

with just the trigger module (standalone mode). The gate width was set to 150 ns The timings were obtained for the ARS stop, ARS valid, as well as the ADC gate by connecting each signal to an oscilloscope. The results are depicted in Fig. 5.5. The ARS valid timing is around 500 ns longer than expected which is an issue. In Fig. 5.1, this timing is shown to be expected to be around 340 ns. At this time, it is not yet understood why this is the case, but it could be due to changes which were made to the trigger firmware in order to make the FPGAs communicate in a timely fashion. This is something that might be looked into further as the preparation progresses. All the other timing information depicted in Fig. 5.5 (relative timing of the ARS stop which is 58 ns, the start of the ADC gate relative to the trigger which is 60 ns) is around what they should be for the DVCS3 experiment.

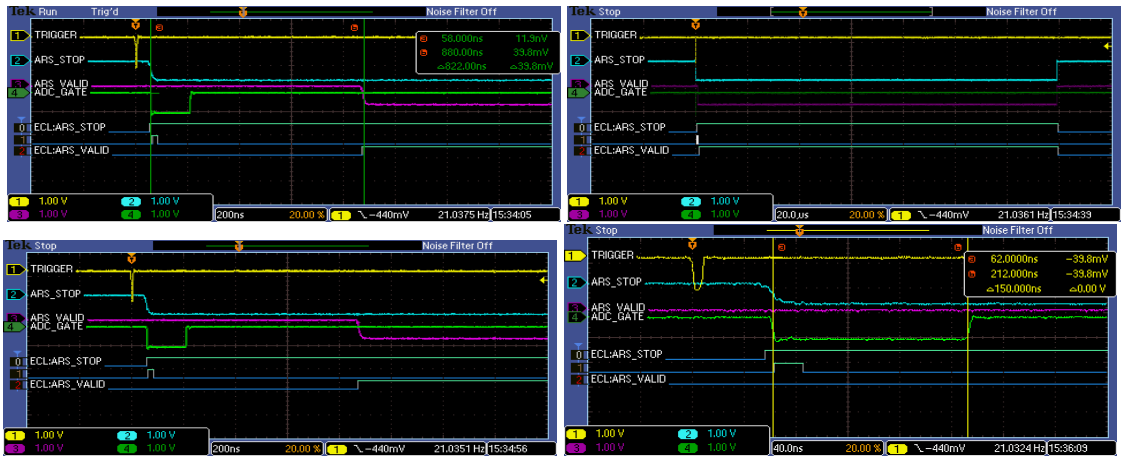

Figure 5.5: Timing measurements of the trigger module. In the four images (the horizontal lines), the yellow line is the trigger, the blue line is the ARS stop, the pink line is the ARS valid, the green line is the ADC gate. The remaining horizontal lines are the ECL signals from the lower daughter boards (with the top and last signals being copies of the ARS stop and ARS valid, while the second being the Master Or). The top-left image shows the relative timing of the ARS stop (which is seen 58 ns after the trigger) and the ARS valid (which is seen 822 ns after the trigger). The top-right image shows that the ARS stop and ARS valid go out to around 140 μs after the trigger is generated. The bottom-left and bottom-right images show the relative timing between the ADC gate with the trigger and the ARS stop. The ADC gate begins 60 ns after the trigger.

5.3.2 Integrity of data

The first step in the testing of the trigger involved using a deterministic pulse generator with the capability to go up to about 100 kHz, though the highest rate used was about 6 kHz since the rates in the actual experiment will not exceed this. Triggering was done on the cosmic input (other inputs could have been chosen). This testing mostly involved looking at the data produced to see if it is as it should be as listed in section 5.2 above.

There were multiple issues that were revealed during these tests - incorrect and changing headerword, zeros in ADC, counters not incrementing as expected. After discovering these issues, the first aim was to try to unravel their cause and have them resolved. Many of these issues were related to issues with the firmware and would show up in different versions of the firmware, sometimes with improvements. The issues were related to the timing of the communication between the FPGAs and the ADCs. Each ADC is instructed by a main FPGA (the control FPGA) on when to send a logic signal to the FPGAs 1, 2 and 3 of Fig. 5.4. This signal tells these FPGAs when to collect data from the ADCs. The trigger control FPGA instructs FPGAs 1, 2 and 3 on when to sample the incoming logic signal from the ADCs. Sampling this signal at the wrong time would corrupt the data stream and this is what appears to have occurred. Solving this issue was a matter of coding the firmware in order to get this timing correct. As it was a firmware issue, this required constant communication with the main engineer of the group who is based in France. The issues were fully diagnosed and communicated with the engineer to see if they could be reproduced in the lab at France. A few of these issues were reproduceable (such as the incorrect and inconsistency of the header word as well as the zeros of the ADCs). The issues that were reproduceable in France were resolved by the engineer. The issues that were not reproduceable in France however had to be resolved at JLab by the JLab staff scientist B. Raydo. Constant testing and communication was also

done with this individual to ensure that the issues were identified and resolved. In addition to the above testing of the firmware, occasionally, the fuses (9 of them) on the trigger had to be replaced.

5.3.3 Dead-time checks

Another check was the dead-time checks. The test was carried out by changing the rate using the deterministic pulse generator and using an oscilloscope to estimate the actual incoming data rate. The result is shown in Fig. 5.6. The results revealed that 50% dead-time is obtained at 6kHz (a dead-time of 167μs). This is unique to this setup as the CPU used was different from what will be used in the hall, the length of the cables throughout the setup was also different - all of these will affect acquisition dead-time.

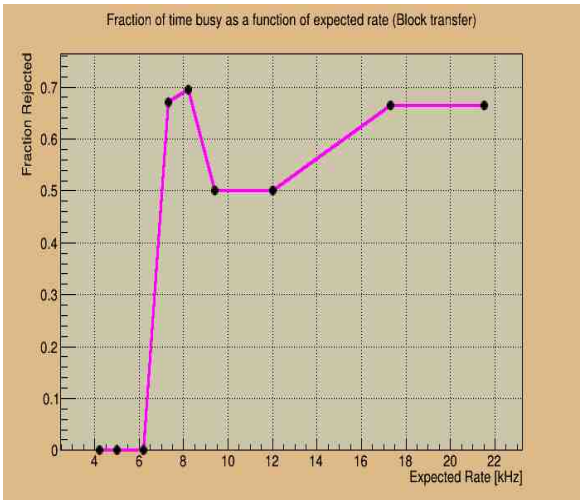

Figure 5.6: Busy time of trigger testing setup in DAQ lab at JLab. As one increases the rate, first, 1 in every 2 events are lost, then 2 in every 3 events and so on. The reason for this pattern is because the DAQ is busy recording a previous event. This is why there is a step-like shape. Notice that events are first lost at around 6 kHz. This result is specific for the DAQ that is being used for this experiment. The results would differ for a different DAQ. The first jump however goes up to 0.7. This is believed to be due to a bad estimate of the actual rate as not much care was taken in estimating errors. However, notice that the expected pattern takes shape afterwards, with 50% of events lost, and then 67%.

5.3.4 Linearity of ADCs

The next step involved investigating the nature of the ADCs - linearity and value of saturation. The value returned by an ADC is proportional to the integral of the signal sent to it up until some point - saturation. This check was necessary in order to ensure that for a given signal, all the ADCs report a similar value. Indeed, the ADC readout are the main input for the trigger on the calorimeter. In order to test the 208 ADC channels, a pulse of fixed width but variable amplitude was sent to each ADC channel using a pulse generator.

The pulse's amplitude was varied using an attenuator. This exponentially decreased the height of the input pulse for each ADC channel. An amplitude that saturated the ADC was first used, then it was gradually adjusted. Fig. 5.7 shows a typical measurement. Two regions are apparent, a linear region (below a relative amplitude of 0.25) and a saturated region (above relative amplitude of 0.25).

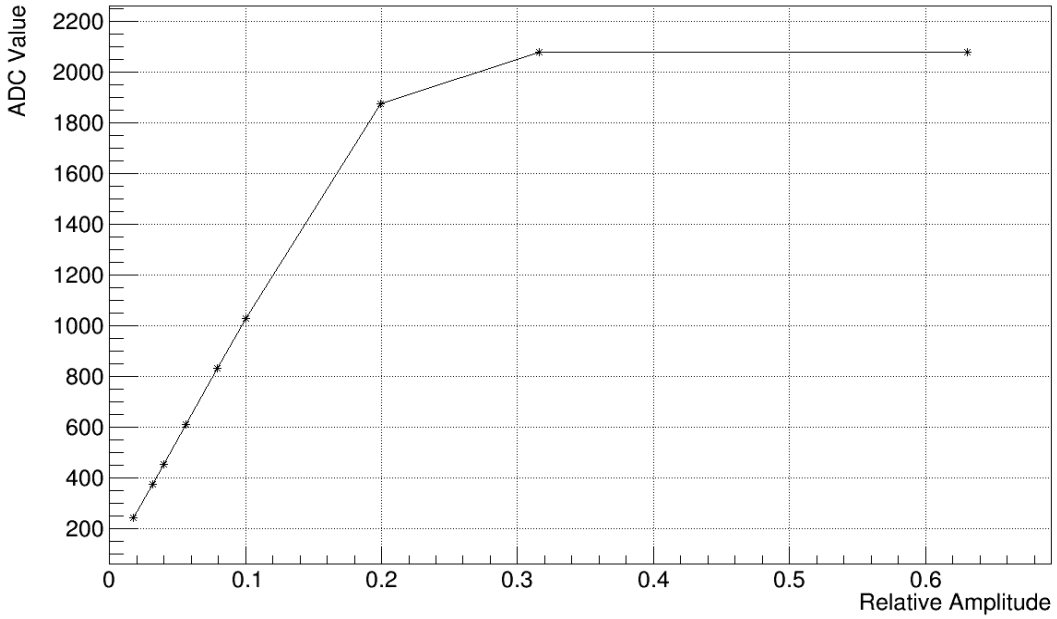

Figure 5.7: The ADC value as a function of relative amplitude is investigated. The ADC digital readout saturates at around 11 bits as expected.

The attenuator used to perform the saturation check above allowed varying of the signal height to ranges that went below the value of saturation thus allowing the possibility of exploring this linearity region. The results of these tests indicated a linear behaviour for all ADCs. The linearity region for each ADC was fit by a polynomial of order 1.

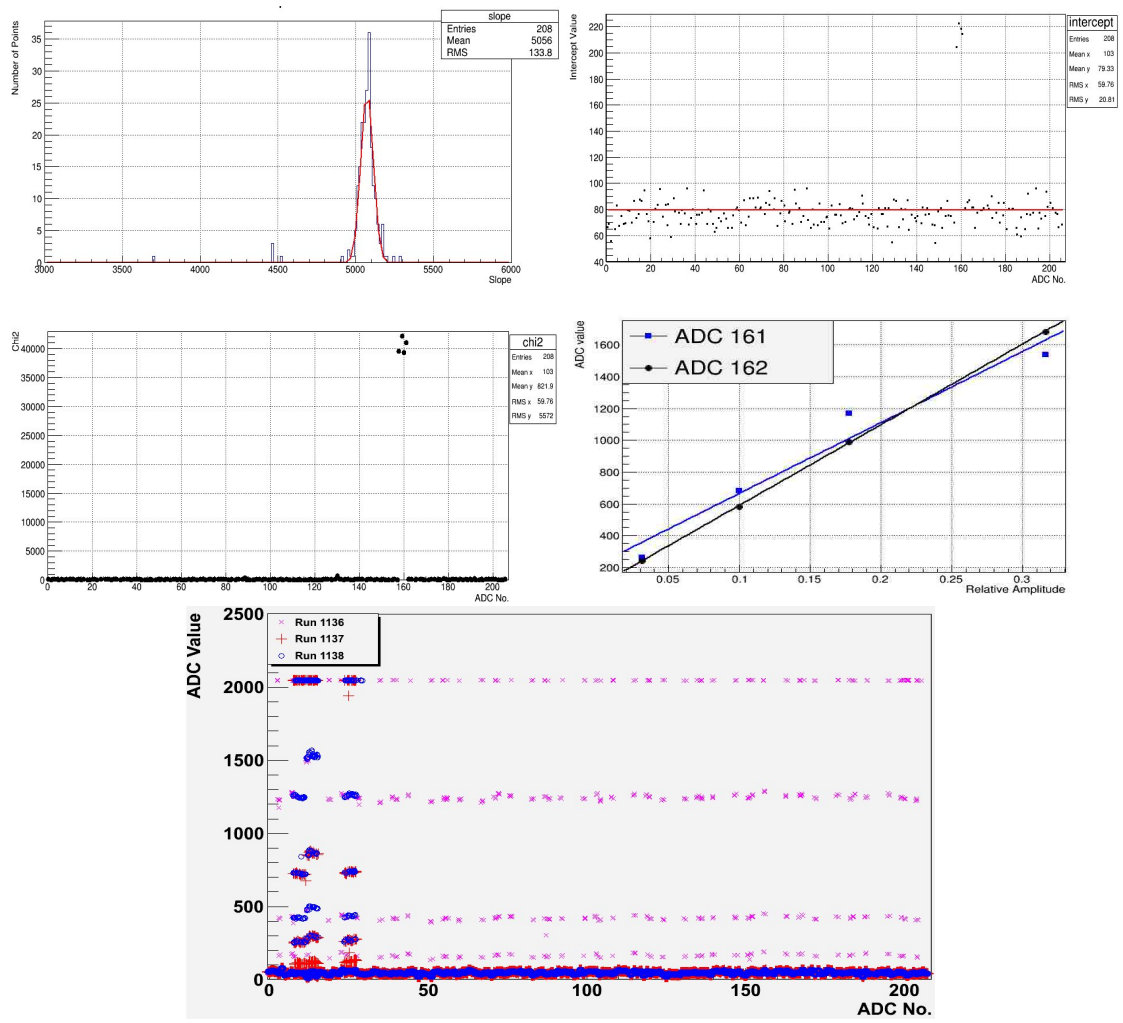

Figure 5.8: Linearity test for the ADCs of the trigger. The top-left plot shows the distribution of the slopes of the fit for each channel. The top-right plot shows the values of the y-intercept as a function of the channel number, the bottom-left plot shows the χ^2 as a function of the channel number. In the bottom-right plot, the blue points (and fit) are the results for ADC 161 which is within the neighborhood of 160 in the two last plots above. The black points (and fit) are the results for one of the good channels (ADC 162). The bottom most plot shows results for all mezzanine boards over different runs for one channel.

In the top-left plot of Fig. 5.8, the distribution of the slopes for the 208 channels is shown. The top-right plot of Fig. 5.8 shows the distribution of the intercept of the fits for all 208 channels. The middle-left plot of Fig. 5.8 shows the χ^2 of the linear fit for the different channels. The middle-right plot of Fig. 5.8 shows one of the bad fits (blue) superimposed on one of the good fits (black). The ADCs with the larger χ^2 behaved like ADC 161 in the last plot in Fig. 5.8 while the ADCs with smaller χ^2 behaved like ADC 162. Note that the first three points (in blue) for ADC 161 seem to be as linear as those for ADC 162 but the last point is significantly far off the fit. This might be due to the ADC saturating earlier when compared with the cases for smaller χ^2. Four ADCs (158-161) have slopes, intercepts and χ^2 significantly different than their pairs - all of them are hosted by the same electronic sub-board (known as a mezzanine). The problem was investigated with the same board at a different location on the motherboard. Since the labeling of the ADC number is related to the location that the mezzanine is placed on the motherboard, the problem will show up on the mezzanine, but the channels for that mezzanine will be labeled differently. This means that with the bad mezzanine at a new location, the channels for that mezzanine (which was labeled 158-161) will now have different labels. In Fig. 5.8 (a plot of the ADC value as a function of the channel number), one sees the effect of the bad mezzanine (mezzanine #00, with channels now labeled 12-15). This plot was obtained by sending a pulse in one channel per mezzanine and attenuating the pulse. The different layers of points correspond to different amounts of attenuation (and thus different relative amplitudes). For all the mezzanines that are good, for a given attenuation, these ADCs are to read about the same value. If one mezzanine is bad, the value for a given attenuation will be noticeably different from the rest of the channels. This is what is seen in Fig. 5.8. The pink points corresponds to the case where a pulse was sent through one channel for each mezzanine. The red and blue points correspond to the case where, after the bad mezzanine was found, the surrounding

mezzanines were scanned to see if signal leakages could cause the same effect on those mezzanines. This was not the case and one can see that none of the surrounding boards are spoiled. As a result, this board will be replaced.

5.3.5 LED and cosmic testing

The next step was to do LED and cosmic tests. The purpose of the tests was to ensure that the trigger is able to correctly perform a sum of the portion of a signal seen in each of four adjacent blocks and correctly compare it with the uniform threshold that was set. There are two possible cluster modes, the first is a single cluster mode where the trigger only considers one cluster. The second mode is the two-cluster mode. In this case, the trigger looks at two non-adjacent clusters.

For the LED tests, a 13×16 LED matrix (Fig. 5.9) was placed inside the calorimeter to illuminate the blocks in such a way, that the signal can be seen by neighboring blocks. This was done by illuminating a single block. A typical signal (arriving inside the integration gate) seen on the oscilloscope looks like that shown in Fig. 5.10. Each block was connected to the trigger. The LED was set to flash at about 6 kHz to do a scan through each block. One can investigate each block by simply telling the LED for that block to turn on. Fig. 5.11 shows the CODA configuration used to perform the tests.

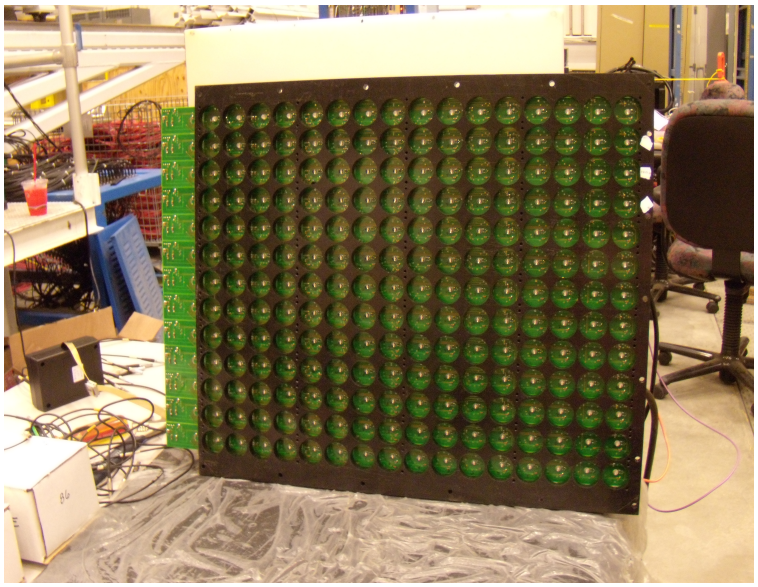

Figure 5.9: The 13×16 LED matrix.

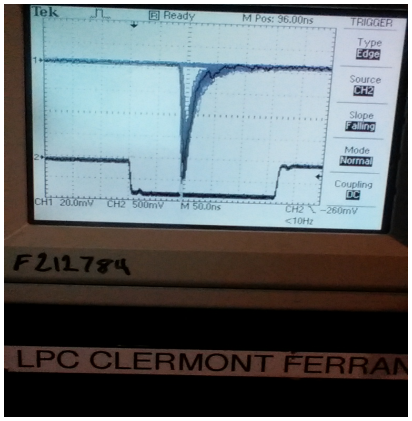

Figure 5.10: A typical integration gate with a signal inside.

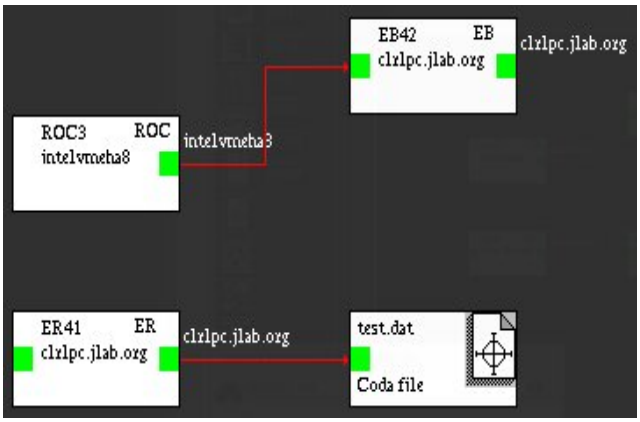

Figure 5.11: CODA configuration used to carry out LED and cosmic testing without the ARSs connected. The upper blocks (from left to right) represent the ROC and event builder. Information is sent from the ROC to the event builder. The lower blocks (from left to right) represent the event recorder and the disk. The event recorder writes the information to the disk.

The cosmic testing involved triggering from the clock input, while waiting for a cosmic to randomly show up. The triggering was around 2 kHz but in general, cosmics only show up around 1% of the time. With the cosmic runs, the functionality of the cluster sum was investigated. There is a word in the data that indicates whether or not a cluster above the set threshold was found see Tab. 5.1. A code was written that computes the cluster sum from the data and compared the result with the result seen by the trigger. There are 3 cases, the first is where the trigger sees a cluster but the code does not find a cluster, the other case is where the code finds a cluster but the trigger does not. The other case is just when the trigger and the code agrees. The code and the trigger should always agree. In the top plot of Fig. 5.12, the result for one of the cosmic runs is displayed. The figure shows there are cases where the code and the trigger disagree. In particular, the case where a cluster is seen by the code but the hardware does not see it turns out to be cases where the FPGA for one set of channels has to exchange information with the FPGA for another set of channels. In Fig. 5.12, the cluster is 142. The bottom plot is the case where the cluster sum is always working.

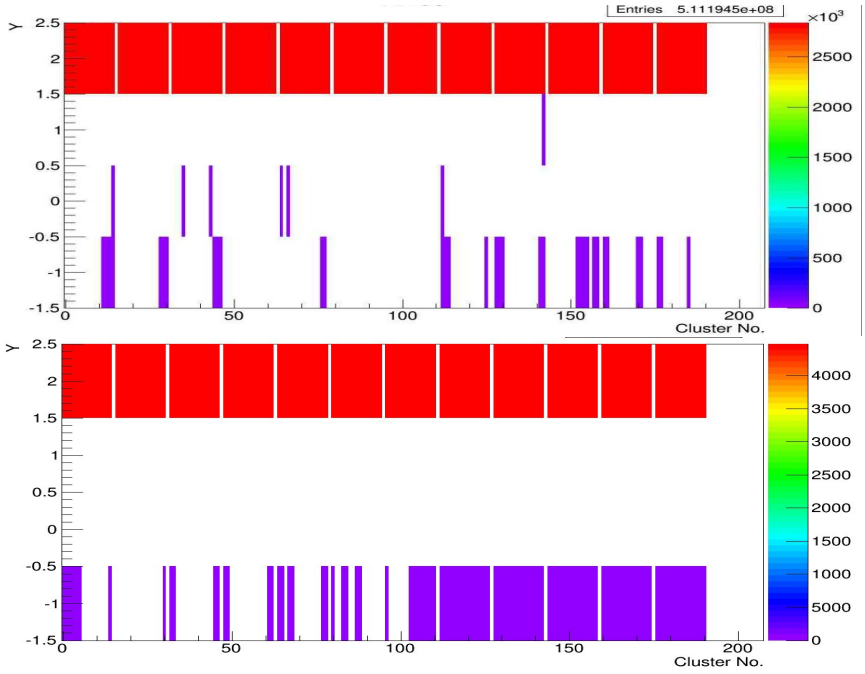

Figure 5.12: June 2014 (top) state and July 2014 (bottom) state of one-cluster sum. Both runs have a threshold of 600. In the case where the $y-axis$ is -1, the code sees a cluster at or above threshold and the trigger agrees. In the case where the $y-axis$ is 0, the hardware detects a cluster above the set threshold but the code does not. In this case, the cluster with the largest value is displayed. In the case where the $y-axis$ is 1, then the code sees a cluster at or above the given threshold but the hardware does not. When the $y-axis$ is 2, the code sees a cluster below threshold and the trigger agrees. The colour scale indicates the number of events. The $x-axis$ represent the cluster number.

5.3.6 Work on ARS modules

The analogue ring sampler (ARS) for the DVCS experiment is a device which contains 128 capacitors that sample continuously, a signal. These samplers are important for the experiment, as they make it possible to resolve cases where events pile onto each other, making them impossible to distinguish from each other. The ARSs allow for the resolving of this pileup due to its high sampling rate of 1 GHz. A typical ARS board for the DVCS experiment is shown in Fig. 5.13.

Figure 5.13: An ARS board used in the DVCS setup. These boards contain 16 channels.

In June 2013 as well as March 2014, work was done on the ARS modules. The work done in June 2013 involved investigating the transfer rate when different number of ARS modules were used. This testing was done with the modules placed in one of the read-out controllers (ROCs). The tests were done using from 1 up to 7 modules and the time it takes to process an event from trigger to conclusion (processing-time) was investigated. This is important for the plan is to use two ROCs. Using two ROCs will increase the processing speed as the ROCs are processed in parallel. The ARS modules perform their readout in series, and as a result, the processing time as a function of the number of modules is expected to be linear. This is indeed what was observed and is shown in Fig. 5.14 where the blue line represents the expected behaviour (processing time = transfer time + conversion time = $138 + 53x$, where x is the number of modules). The behaviour displayed indicates that for the upcoming experiment, it is possible to use 7

boards in one ROC. With a total of 13 boards required, the configuration with two ROCs is 6 boards in one ROC and 7 boards in another.

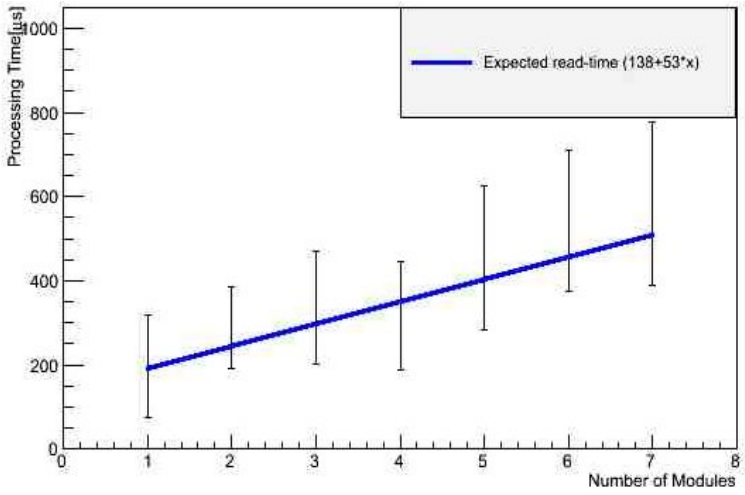

Figure 5.14: Processing time (in μs) as a function of the number of modules. The upper bound on the error bar is determined from the lowest rate at which one was missing every other event and the lower error bar determined from the highest rate where no event was missed. The blue line is the expected behaviour.

In March 2014, the ARS readout was found to be corrupted. This problem arose with 13 boards in one crate. Each board has to be initialized before it can give any sensible readout but the pedestal readouts in some channels read 4000. The pedestals are typically supposed to read a value of about 2000. This issue was discovered by Frederic Georges, an intern at JLab. The top plot of Fig. 5.15 (courtesy of Frederic) shows this behaviour.

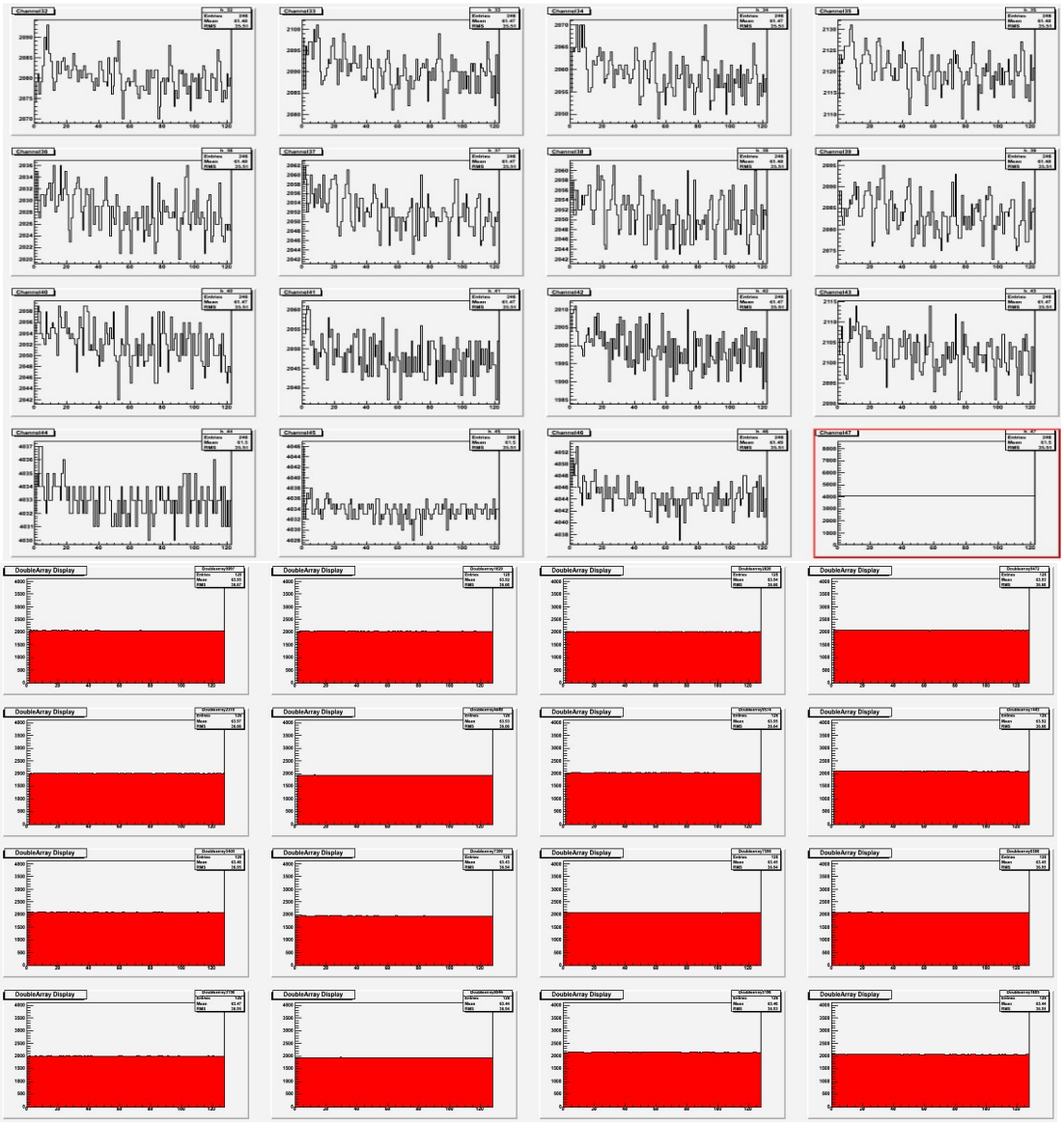

Figure 5.15: ARS initialization problem. The top plot reflects the state of the ARS on March 2014 while the bottom plot reflects the state of the ARS as of August 2014. The last four bottom channels in the top plot read 4000. All the channels in the bottom plot read 2000 as they should.

The problem was later resolved with the assistance of JLab staff scientist and DVCS group member, Alexandre Camsonne. The problem later went away when most of the boards were removed and reinserted tightly into the crate so as to ensure the connectors 'see' the back plane of the crate. This implied that the problem was due to an ARS board

not properly connected to the back plane of the crate. The state as of August 2014 displayed in the bottom plot of Fig. 5.15. Notice that all the pedestals are reading 2000 as expected. Finally, the 13 ARS boards, trigger and calorimeter were connected and tested together in order to check that as a whole, the system is functional. The trigger and ARS data was checked and the pedestals and header word was correct.

5.3.7 Summary of Results

Overall, the following work was completed on the trigger

- The ARS stop comes 58 ns after the trigger while the ARS valid is 822 ns after the trigger (300 ns longer than expected). The ADC gate is 60 ns after the trigger.
- Data integrity - The data stream is looking as it should (header word is correct, ADCs are all reading non-zero values, pedestals look stable, counters are incrementing correctly).
- Linearity of ADCs - The ADCs are behaving linearly and are saturating where expected, however, there seems to be some issues with the uniformity of this behaviour for the channels of mezzanine 00 seem to be giving larger outputs than expected, but seems to saturate at the same amount as the others.
- The trigger starts to lose events when they arrive at a rate of 6kHz. This is unique to the setup done for this test and might not be the same in a different setup.
- Cluster sum - The single cluster sum is working correctly. The two cluster sum feature is not yet functional.

6 Conclusion and Future work

Exploring the DVCS process will allow a clean mapping of the position and momentum distribution of quarks and gluons inside hadrons. This structure will be unraveled using the newly developed tools of GPDs. The DVCS3 experiment will aim to prove the dominance of leading twist terms, where one scatters from a single quark. This will be done by expanding the Q^2 range of the last experiment, taking advantage of the 12 GeV upgrade.

In this thesis, some basic background regarding QCD and how the DVCS experiment will add to this knowledge was given. Then, a brief introduction to data acquisition systems was given and this was related to the data acquisition system being prepared for the current DVCS experiment. Finally, the preparation of the trigger as well as the ARS was explained. The trigger will select events where a photon at or above 1.5 GeV detected in the 13×16 PbF_2 calorimeter in coincidence with an electron detected in the left HRS. This will reduce acquisition dead-time which will help to improve on the measurement of the cross-section. It is hoped that during this experiment, cross-section measurements will be made down to 4%.

The trigger arrived at JLab in September 2013. Work on the trigger for this thesis began in January 2014. For about 4.5 months, the trigger had issues with the integrity of the data. This was a firmware issue which was later resolved through constant communication with the main engineer, Magali Magne and JLab staff scientist B. Raydo. While work was being done, there were two main deadlines - one for the electronics review (May 20, 2014) and the other deadline for getting the trigger to be functional (July 25, 2014). The plan is for the experiment to begin in October 2014 and it seems this deadline is currently within reach.

The work that was completed in time for the electronics review involved fixing the issues with the data integrity. The issues with data integrity that arose were: incorrect and

inconsistent header word, most ADCs read zeros and would sometimes all read the same value when they read non-zero. These issues were resolved by Magali Magne and B. Raydo by improving on the firmware - fixing the timing of the communication between the ADCs and the FPGAs.

Preparation of the ARS modules was also done in time for the electronics review. Some of the work for the ARS started in June 2013 but in February 2014, the ARSs had a problem with initialization. In this situation, the channels of some of the ARS modules would read a value of 4000 when in actuality, they are supposed to read 2000 for their pedestals. The issue was discovered by Frederic Georges, a JLab intern and was later fixed with the assistance of Alexandre Camsonne, a JLab staff scientist and member of the DVCS group. The problem appeared to have been due to a badly connected board.

Other work done by the electronics review deadline involved checking the linearity of the ADCs as well as checking the dead-time of the trigger module. The ADCs were mostly found to be linear, except four which share the same mezzanine board (mezzanine 00). The ADCs were also found to saturate at 11 bits. For the dead-time check, the setup which was used resulted in a loss of events starting at around 6 kHz. This is good but is unique to the setup and might be different when the setup is done in the hall.

For the functionality deadline of July 25, 2014, the main focus was to get the quadrature sum working. Recall that the DVCS trigger works by summing the signals produced by a photon (in coincidence with an electron in the left HRS) in four adjacent blocks and comparing with a threshold corresponding to a 1.5 GeV photon. The quadrature sum issue was a firmware issue which was resolved by the JLAB staff scientist B. Raydo. The testing for this was done using LEDs and cosmics. In addition, testing was done with the trigger, ARS and calorimeter cabled together. All the ARS channels were reading their expected pedestals of around 2000 and the trigger was functional in that

clear signals were seen in the channels, the integrity of the data looked good and the quadrature sum was functional.

In addition, timing measurements were made with the assistance of Paul King. These measurements were done to check if the timing will meet the expectations of the experimental setup. It was found that the ARS valid signal was generated 500 ns longer (after the ARS stop) than expected. A possible reason for this could be that the changes which were made to get the trigger to work might have affected this time. It is unsure how serious of a problem this is at this time.

The next step is to set up the system inside the hall (in progress). Once this is done, the read-out time with the ARSs, trigger and HRS connected. Dead-time scalers will also be checked and the dead-time corrections as a function of DAQ rate with the entire system will be tested.

Finally, in October 2014, the experiment will begin. Although some work still needs to be completed, the deadline seems to be within arms reach.

References

[Ber11] Sylvia Berryman. Ancient atomism. In Edward N. Zalta, editor, *The Stanford Encyclopedia of Philosophy*. Winter 2011 edition, 2011.

[BR05] A.V. Belitsky and A.V. Radyushkin. Unraveling hadron structure with generalized parton distributions. *Physics Reports*, 418(16):1 – 387, 2005. URL: http://www.sciencedirect.com/science/article/pii/S0370157305002644, doi:http://dx.doi.org/10.1016/j.physrep.2005.06.002

[Cam05a] Carlos Muñoz Camacho. *Diffusion Compton profondément virtuelle dans le Hall A au Jefferson Laboratory*. PhD thesis, l'Université Paris VI, December 2005.

[Cam05b] Alexandre Camsonne. *Experimental setup for Deeply Virtual Compton Scattering (DVCS) experiment in Hall A at Jefferson Laboratory*. PhD thesis, Universite Blaise Pascal, November 2005.

[DPE13] Maurizio Di Paolo Emilio. *Data Acquisition Systems: From Fundamentals to Applied Design*. Elsevier, 2013.

[eatHADC00] Y. Roblin et al (the Hall A DVCS Collaboration). Deeply Virtual Compton Scattering at 6GeV, 2000. E00-110 JLab, Accessed:2014-04-02. URL: http://hallaweb.jlab.org/experiment/DVCS/dvcs.pdf

[eatHADC03] E. Voutier et al (the Hall A DVCS Collaboration). Deeply Virtual Compton Scattering on the Neutron, 2003. E03-106 JLab, Accessed:2014-06-07. URL: http://hallaweb.jlab.org/experiment/DVCS/ndvcs.pdf

[Gri04a] David Griffiths. *Introduction to Elementary Particles: 1st Edition*. WILEY-VCH Verlag GmbH and Co. KGaA, 2004.

[Gri04b] David Griffiths. *Introduction to Quantum Mechanics: 2nd Edition*. WILEY-VCH Verlag GmbH and Co. KGaA, 2004.

[Gui05] M. Guidal. Deep virtual compton scattering and the nucleon generalized parton distributions. *Nuclear Physics A*, 751(0):180 – 191, 2005. Proceedings of the 22nd International Nuclear Physics Conference (Part 1). URL: http://www.sciencedirect.com/science/article/pii/S037594740500103X, doi:http://dx.doi.org/10.1016/j.nuclphysa.2005.02.011

[HW07] Charles E. Hyde-Wright. Outlook for Generalized Parton Distributions and Deeply Virtual Compton Scattering in Hall A, 2007. Accessed:

2014-07-25. URL: http://hallaweb.jlab.org/experiment/DVCS/documents/talk/CEH_jan07_DVCS_hallAmeet.pdf

[JLa] JLab. 12 GeV Upgrade Technical Scope - Physics Experimental Equipment. Accessed: 2014-07-20. URL: http://www.jlab.org/12GeV/scope_equipment.html

[JLa13] JLab. 12 GeV Upgrade Technical Scope, 2013. Accessed: 2014-08-07. URL: http://www.jlab.org/div_dept/physics_division/GeV/index.html

[Leo94] W. L. Leo. *Techniques for Nuclear and Particle Physics Experiments: A How-To Approach, Second Revised Edition*. Springer-Verlag Berlin Heidelberg GmbH, 1994.

[LHAC06] Jefferson Lab Hall A Collaboration. Measurements of the Electron-Helicity Dependent Cross Sections of Deeply Virtual Compton Scattering with CEBAF at 12 GeV. 2006. E12-06-114 JLab. arXiv:nucl-ex/0609015.

[Roc14] Julie Roche. Deeply Virtual Compton Scattering in Hall A at Jlab, 2014. Accessed: 2014-08-02. URL: http://hallaweb.jlab.org/experiment/DVCS/

[Rov04] Carlo Rovelli. *Quantum Gravity*. Cambridge University Press, 2004.

[TM02] Inc The MathWorks. Data acquisition toolbox:for use with matlab, 1999-2002. Accessed: 2014-02-10. URL: http://radio.feld.cvut.cz/matlab/pdf_doc/daq/daqug.pdf